Draft version November 12, 2025
Typeset using LaTeX **twocolumn** style in AASTeX63

The Deepest GLIMPSE of a Dense Gas Cocoon Enshrouding a Little Red Dot

Vasily Kokorev,[1,2] John Chisholm,[1,2] Rohan P. Naidu,[3] Seiji Fujimoto,[4,5] Hakim Atek,[6] Gabriel Brammer,[7] Steven L. Finkelstein,[1,2] Hollis B. Akins,[1,2] Danielle A. Berg,[8,2] Lukas J. Furtak,[1,2] Qinyue Fei,[4] Tiger Yu-Yang Hsiao,[1,2] Jorryt Matthee,[9] Julian B. Muñoz,[1,2] Pascal A. Oesch,[10,7] Richard Pan,[11] Pierluigi Rinaldi,[12] Alberto Saldana-Lopez,[13] Daniel Schaerer,[14,15] Marta Volonteri,[6] and Adi Zitrin[16]

[1] *Department of Astronomy, The University of Texas at Austin, Austin, TX 78712, USA*
[2] *Cosmic Frontier Center, The University of Texas at Austin, Austin, TX 78712, USA*
[3] *MIT Kavli Institute for Astrophysics and Space Research, 70 Vassar Street, Cambridge, MA 02139, USA*
[4] *David A. Dunlap Department of Astronomy and Astrophysics, University of Toronto, 50 St. George Street, Toronto, Ontario, M5S 3H4, Canada*
[5] *Dunlap Institute for Astronomy and Astrophysics, 50 St. George Street, Toronto, Ontario, M5S 3H4, Canada*
[6] *Institut d'Astrophysique de Paris, CNRS, Sorbonne Université, 98bis Boulevard Arago, 75014, Paris, France*
[7] *Cosmic Dawn Center (DAWN), Niels Bohr Institute, University of Copenhagen, Jagtvej 128, København N, DK-2200, Denmark*
[8] *Department of Astronomy, The University of Texas at Austin, 2515 Speedway, Stop C1400, Austin, TX 78712, USA*
[9] *Institute of Science and Technology Austria (ISTA), Am Campus 1, 3400 Klosterneuburg, Austria*
[10] *Département d'Astronomie, Université de Genève, Chemin Pegasi 51, 1290 Versoix, Switzerland*
[11] *Department of Physics & Astronomy, Tufts University, MA 02155, USA*
[12] *Steward Observatory, University of Arizona, 933 North Cherry Avenue, Tucson, AZ 85721, USA*
[13] *Department of Astronomy, The Oskar Klein Centre, Stockholm University, AlbaNova, SE-10691 Stockholm, Sweden*
[14] *Observatoire de Genève, Université de Genève, Chemin Pegasi 51, 1290 Versoix, Switzerland*
[15] *CNRS, IRAP, 14 Avenue E. Belin, 31400 Toulouse, France*
[16] *Department of Physics, Ben-Gurion University of the Negev, P.O. Box 653, Be'er-Sheva 84105, Israel*

(Received n/a; Revised n/a; Accepted n/a)

Submitted to ApJ

ABSTRACT

The detection of strong Balmer breaks and absorption features in Little Red Dots (LRDs) suggests they host AGN embedded within dense gas envelopes, potentially powered by super-Eddington accretion. We present GLIMPSE-17775, a luminous ($L_{\rm bol} \sim 10^{45}$ erg s^{-1}) LRD at $z = 3.501$ behind Abell S1063 ($\mu \sim 2$), observed with deep *JWST*/NIRCam and a ∼20 hr (80 hr de-lensed) NIRSpec/G395M spectrum. The data reveal 40+ emission and absorption features, including a rich forest of low-ionization Fe II lines and numerous broad hydrogen recombination transitions. We use this depth to test the dense-gas interpretation through five independent diagnostics. Nearly all permitted lines show exponential wings with consistent FWHM, the signature of Thomson scattering requiring $n_e \gtrsim 10^8$ cm^{-3}. Adopting this width yields $M_{\rm BH} \sim 10^{6.7} M_\odot$, a factor of ten lower than Gaussian fits, and $\lambda_{\rm Edd} \sim 1.8$. Additional diagnostics support the same picture: a pronounced Balmer break ($f_{\nu,4050}/f_{\nu,3670} = 2.0 \pm 0.1$), enhanced He I λ7065 and λ10830 with P-Cygni absorption, Bowen-fluorescent O I λ8446–λ11290 emission requiring Lyβ pumping, and 16 Fe II lines matching fluorescence models. These features indicate a dense ($n \sim 10^8$ cm^{-3}), partially ionized cocoon where scattering and fluorescence dominate line formation, providing strong evidence that at least some LRDs are powered by super-Eddington black-hole growth in the early Universe.

Keywords: High-redshift galaxies (734), Early universe (435)

1. INTRODUCTION

Corresponding author: Vasily Kokorev
vkokorev@utexas.edu

One of the most enticing puzzles brought upon by the launch of the *James Webb Space Telescope* (*JWST*) has been the discovery of red, compact objects called "Little Red Dots" (LRDs; Matthee et al. 2023). Previously invisible to the *Hubble Space Telescope* (*HST*) due to their extreme faintness in the optical and lack of near-infrared (NIR) coverage, LRDs have emerged in abundance (Kokorev et al. 2024a; Kocevski et al. 2024; Akins et al. 2024; Barro et al. 2024) thanks to unprecedented NIR sensitivity of *JWST*.

Their unusual properties—such as compact morphologies in rest-optical and distinctive "v-shaped" spectral energy distributions (SEDs)—make LRDs easy to identify in *JWST* fields, however this is where the simplicity ends. Explaining LRDs as either evolved or dusty compact galaxies proves difficult: the former scenario requires massive stellar populations that strain ΛCDM predictions (Labbé et al. 2023a; Boylan-Kolchin 2023), while the latter implies significant dust emission—yet none is observed (Labbé et al. 2023b; Casey et al. 2024; Akins et al. 2024; Leung et al. 2024).

Over time, the accumulating detections of broad Balmer series emission lines (Kocevski et al. 2023, 2024; Matthee et al. 2023, just to name a few), often accompanied by signatures of extreme ionization (e.g., Kokorev et al. 2023), have begun to clarify the physical origin of LRDs, pointing increasingly toward AGN as the underlying power source. In parallel, the much-needed advent of NIRSpec MSA programs based on red targets selected from JWST imaging (e.g., de Graaff et al. 2025a) has provided critical confirmation: nearly all point sources exhibiting "v-shaped" spectral energy distributions (SEDs) reveal broad emission lines upon spectroscopic follow-up (Hviding et al. 2025), solidifying their AGN interpretation.

The nature of the spectral inflection point in LRDs, typically located near ~ 3600 Å, has also undergone significant revision. Initially interpreted as a stellar Balmer break (Labbé et al. 2023a), this feature implied implausibly high stellar masses (M_*) far too early in cosmic history (Boylan-Kolchin 2023; Sabti et al. 2024). A second hypothesis invoked differential dust attenuation and host galaxy contamination in the rest-UV to explain the sharp discontinuity (Volonteri et al. 2025). However, this explanation was soon ruled out by Setton et al. (2024); Ma et al. (2025), who demonstrated that the break generally lies around the Balmer limit, albeit with a fundamentally different origin than initially proposed.

More recently, a series of theoretical and observational works have converged on a new picture: that LRDs may host accreting black holes enshrouded in exceptionally dense, partially ionized gas cocoons—the so-called Black Hole Star (BH*) scenario (Inayoshi & Maiolino 2025; Naidu et al. 2025; Taylor et al. 2025; de Graaff et al. 2025b). In this framework, the steep Balmer-limit break, blueshifted absorption, and suppressed X-ray and radio emission (e.g Naidu et al. 2025; Inayoshi & Maiolino 2025) all arise naturally from a radiation-dominated, optically thick environment surrounding a rapidly growing black hole, while the UV emission and forbidden optical lines (e.g. [O III] $\lambda\lambda 4959, 5007$) potentially originate from the extended host. The dense-gas interpretation also offers a natural explanation for the P-Cygni-like Balmer and helium profiles frequently seen in high-S/N spectra (Matthee et al. 2023), the non-Gaussian, exponentially-winged line shapes predicted by radiative-transfer models of scattering in ionized gas (Rusakov et al. 2025; Chang et al. 2025) and Lymanα - like resonantly scattered shapes (Chang et al. 2025; Naidu et al. 2025). Intriguingly, if electron and resonant scattering indeed dominate the broad-line widths, then the true virial velocities (traced by intrinsically narrower Gaussian core)—and hence black-hole masses—could be lower by an order of magnitude, alleviating the apparent tension between LRD black-hole masses and their compact host galaxies (Rusakov et al. 2025).

So far, however, the BH* / dense-gas interpretation of LRDs has relied largely on the Balmer break, occasional absorption features (Lin et al. 2025a), and, to a limited extent, the shapes of broad emission lines (Rusakov et al. 2025). While these features are consistent with the presence of dense, partially ionized gas, they stop short of providing direct spectroscopic confirmation of the physical conditions expected by the BH* scenario. What has been missing is an unambiguous demonstration—through emission-line physics—that LRDs indeed host dense, optically thick cocoons surrounding rapidly accreting black holes. Such evidence would directly tie the observed line formation, excitation, and radiative transfer to dense, stratified envelopes of gas, surrounding the central engine.

In this work, we present precisely such a case: an exceptionally deep ∼20 hr, equivalent to 80 hr without lensing magnification, *JWST*/NIRSpec G395M spectrum of a luminous LRD at $z = 3.50102$. The target, GLIMPSE-17775, lies in a highly magnified region of the massive galaxy cluster Abell S1063 (AS1063 hereafter) and benefits from the combined power of *JWST*/NIRCam imaging from the GLIMPSE GO program (PID 3293; PIs H. Atek & J. Chisholm) and recent NIRSpec spectroscopy from the GLIMPSE-D DDT program (PID 9223; PIs S. Fujimoto & R. Naidu). This synergy of ultra-deep spectroscopy and strong gravitational lensing enables an unprecedented view of GLIMPSE-

17775, revealing rest-frame optical and near-infrared features at a level unseen before in any LRD. We detect over forty emission and absorption features—sixteen of them Fe II transitions forming a dense "iron forest." The remarkable richness of this spectrum makes GLIMPSE-17775 a uniquely powerful laboratory for dissecting the dense, radiation-dominated environments that accompany early black-hole growth.

This paper is organized as follows. In Section 2 we present the GLIMPSE-D NIRSpec dataset alongside the photometric data sets used in this study. In Section 3 we calculate the spectroscopic redshift, describe the identification of prominent emission/absorption features and describe bespoke fitting of various line complexes. Section 4 describes the measurement of the source morphology, dust attenuation and black hole masses. In Section 5 we comment on the various properties of the emission features in the our target and finally discuss our findings in Section 6.

Throughout this work we assume a flat ΛCDM cosmology with $\Omega_{m,0} = 0.3$, $\Omega_{\Lambda,0} = 0.7$ and $H_0 = 70$ km s^{-1} Mpc^{-1}, and a Chabrier (2003) IMF between $0.1 - 100$ $M_\odot$. All magnitudes are expressed in the AB system (Oke 1974).

2. OBSERVATIONS AND DATA

The target - GLIMPSE-17775 was originally identified as a bright LRD candidate in the *JWST* NIRCam imaging captured by the GLIMPSE (PID: 3293; PIs: H. Atek & J. Chisholm) survey (H. Atek in prep.) of the lensed AS1063 Hubble Frontier Field (Lotz et al. 2017). The highly magnified area of AS1063 has already successfully yielded $z > 16$ galaxy candidates (Kokorev et al. 2025), potential Population III hosts (Fujimoto et al. 2025), numerous faint and high-redshift galaxies (Chemerynska et al. 2025), new constraints on reionization (Korber et al. 2025), identification of intermediate mass black-holes (Fei et al. 2025), and a wide variety of enigmatic LRDs, some moderately lensed. The LRD selection was based on the standard compactness plus "v-shape" criteria already laid out in Labbé et al. (2023b); Greene et al. (2024); Akins et al. (2024); Kokorev et al. (2024a), using the photometric redshifts derived with EAZY (Brammer et al. 2008), a technique that has proven successful at consistently identifying many exciting sources (see e.g. Taylor et al. 2025; Kokorev et al. 2023; Naidu et al. 2025; de Graaff et al. 2025b; Akins et al. 2025). The LRD in question - GLIMPSE-17775 located at $z_{\rm phot} = 4.2 \pm 0.1$, stood out in particular due to its extreme rest-optical brightness with $m_{\rm f444w} \sim 23.6$ mag and a modest lensing magnification $\mu \sim 2$. Very little could be done with photometry alone, however this marked GLIMPSE-17775, as a promising target for any future spectroscopic follow-up.

2.1. *Photometry*

We use photometry both to select targets for the GLIMPSE-D NIRSpec observations and, during spectroscopic modeling, to constrain the overall shape of the SED and correct for NIRSpec slit losses. In addition to *JWST*/NIRCam data, we incorporate deep *HST* ACS and WFC3 imaging from the Hubble Frontier Fields (HFF; Lotz et al. 2017) and BUFFALO (Steinhardt et al. 2020) programs. Our reprocessed *HST* mosaics are based on Gaia-aligned images from the CHArGE archive (Kokorev et al. 2022), hosted on the Dawn JWST Archive (DJA; Valentino et al. 2023). More descriptions of the image reduction and source extraction procedure can be found in Endsley et al. (2024), as well as in the upcoming GLIMPSE overview paper by H. Atek et al. (in prep), we briefly summarize the latter procedure below.

Photometry is performed on PSF-homogenized *HST* and *JWST* images, convolved to the resolution of the F480M filter. Source detection is carried out using SExtractor (Bertin & Arnouts 1996) through two parallel steps. We construct two inverse-variance-weighted detection images: one from the short-wavelength (SW; F090W, F115W, F150W, F200W) bands to preserve spatial resolution, and one from the long-wavelength (LW; F277W, F356W, F444W) bands to ensure sensitivity to red or dusty sources (e.g., LRDs). Unlike the science images, these have not been PSF matched. These SW and LW detection catalogs are subsequently merged into a single, combined catalog. Photometry is then measured using PHOTUTILS (Bradley et al. 2020) in a range of circular apertures ($D = 0\farcs1$–$1\farcs2$). Photometric uncertainties are estimated by placing random apertures in empty regions around each source. Unless stated otherwise, we adopt total fluxes measured within a $D = 0\farcs2$ aperture throughout this work.

2.2. *NIRSpec Observations*

GLIMPSE DDT (GLIMPSE-D hereafter) NIRSpec data were obtained during a campaign (DDT #9223 PIs: S. Fujimoto & R. Naidu) to study a promising Population III galaxy candidate (Fujimoto et al. 2025). GLIMPSE-D obtained a total of 3 G395M/F295LP MSA pointings, totaling 29.78h of total exposure time. The pointing center was different for all three configurations to maximize the total object yield. In total,the GLIMPSE-D sample contains 384 spectra with depths varying from 9.2h to $\sim$ 30h. All of the planned observations were successfully executed between June 30 and

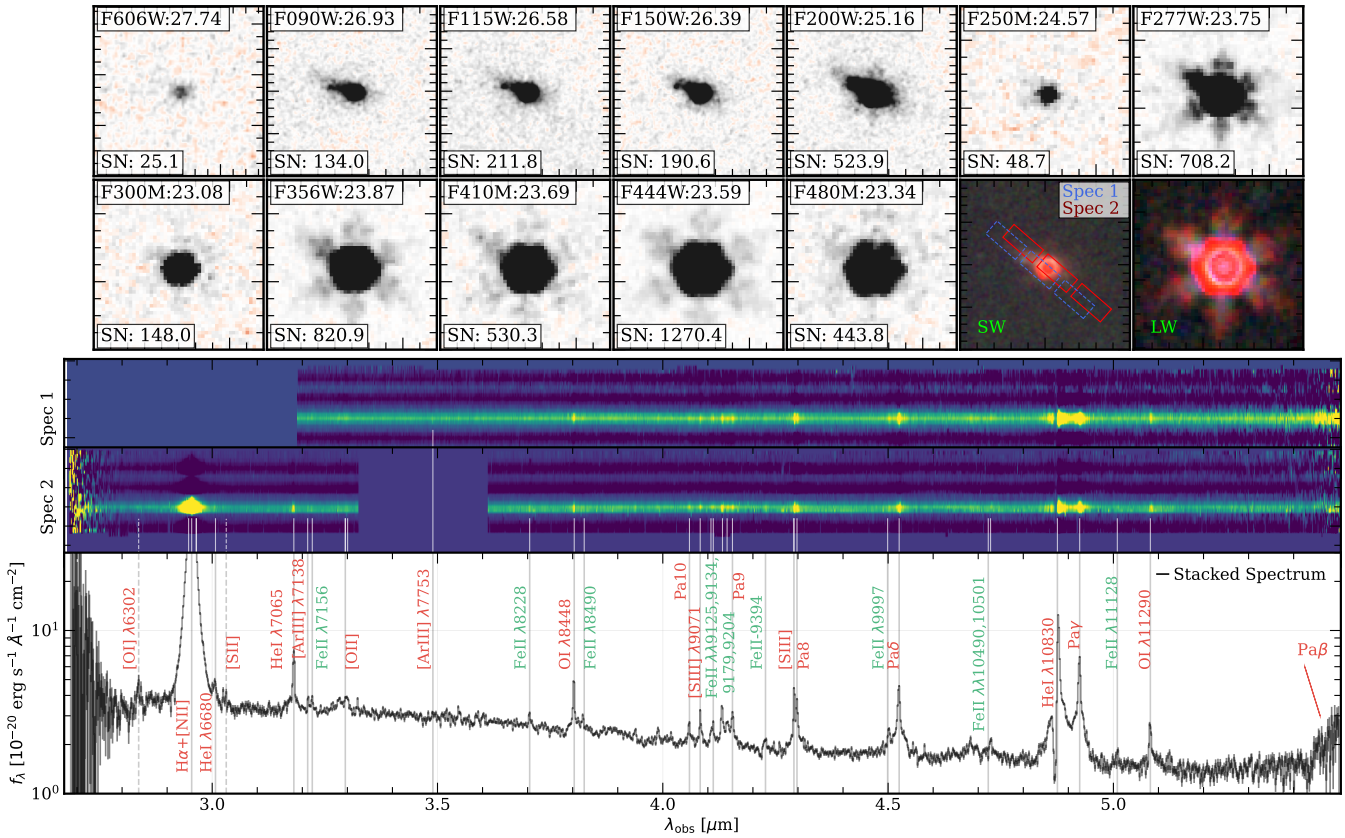

Figure 1. Top: *JWST*/NIRCam and *HST* 2.″0 stamps and the RGB short (SW) and long wavelength (LW) color images comprised of the F115W, F150W, F200W and F277W, F356W, and F444W bands, respectively. MSA shutters for both configurations covering GLIMPSE-17775 are shown in blue and red, respectively. The source morphology is resolved and extended up to $\sim 2\mu$m, and then appears to transition to a more PSF-dominated and compact shape, echoing a growing sample of LRDs with extended rest-UV morphology (Matthee et al. 2023; Rinaldi et al. 2025a; Juodžbalis et al. 2024; Labbe et al. 2024) Thus likely hinting at a presence of the host-galaxy in the filters covering rest-UV. In each panel we show the total AB magnitude as presented in the GLIMPSE catalog (Kokorev et al. 2025, H. Atek in prep.). The source is exceptionally bright (M444$\sim$ 23.6) and is detected in most *JWST* bands at $> 100\sigma$. **Middle:** 2D MSA G395M spectra covering GLIMPSE-17775. **Bottom:** Combined 1D spectrum (for extraction method see e.g. Kokorev et al. 2023; de Graaff et al. 2024) of the LRD in the observed frame. We show the data in black, and the uncertainty with a black shaded region. Fixing the systemic redshift to the [S III] λ9071 line - $z_{\rm spec} = 3.50102 \pm 0.00019$ - we show the positions and label the prominent emission with significant ($\geq 3\sigma$) detections as solid vertical lines. Iron lines are shown separately in green. Due to the sheer number of features, not all could be labeled, we show all of them in Figure 2. Emission lines for which we only obtain an upper limit are shown with dashed lines.

July 2 2025. For each MSA configuration, GLIMPSE-D employed a standard 3-point nod pattern at an aperture position angle `PA_V3` = 270.5°, using 494 groups per integration with the NRSIRS2 readout mode. The full details of the target selection, prioritization and MSA planning will be presented in a forthcoming survey paper (Fujimoto. S & Naidu. R., et al in prep.).

2.3. *G395M Data Reduction and Calibration*

The GLIMPSE-D MSA spectra were uniformly reduced using MSAEXP (v0.9.8; Brammer 2022). This procedure starts with the level-2 calibrated products obtained from MAST and applies a number of corrections that include 1/f noise, artifact detection and removal and a bias correction in individual exposures (see e.g. Rigby et al. 2023, for more details). Together with the *JWST* pipeline MSAEXP sets the slit WCS, performs flat-fielding and computes an initial pass-loss correction. Each one of the 2D shutters in then drizzled onto a common pixel grid. Using the standard approach, the background subtraction is performed locally by using the stacked, source-free shutters. The 1D spectra are then obtained by using the optimal extraction method (e.g. de Graaff et al. 2023; Arrabal Haro et al. 2023), where the center and width of the extraction "aperture" varies depending on the best fit Gaussian model (Horne 1986); similar to the methodology which has been widely adopted by a variety of other works (e.g. Wang et al. 2023; Greene et al. 2024; Kokorev et al. 2024b).

The absolute flux calibration of MSA spectra can be influenced by several factors, including the position of the source within the shutter, calibration and astrometric uncertainties, and the intrinsic morphology of the source. To correct for these effects and derive an overall slit-loss correction, we rescale the extracted 1D spectra by convolving them with all available NIRCam filters and comparing the resulting flux densities to the total photometry from the GLIMPSE catalog. A wavelength-dependent correction is then obtained by fitting a second-order polynomial to these differences.

The target in this paper was observed in all three configurations, however one of them is severely contaminated by sources in the same row, making the data recovery for this source unfeasible. Despite that, GLIMPSE-17775 is securely detected in two configurations (33262s and 40703s), making the total integration time 20.55h. We combine the extracted and separately calibrated 1D spectra by using inverse-variance weighting. We show the stacked spectrum in Figure 1.

3. EMISSION LINE ANALYSIS

3.1. *Spectroscopic Redshift*

The spectrum of GLIMPSE-17775 reveals a staggering wide variety of significantly detected emission and absorption lines. Before focusing on individual features and their complex components, we perform an initial tally of all detectable lines using a heavily modified version of MSAEXP (Brammer 2022; Kokorev et al. 2024b). The key modifications allow the ability to vary the line widths, as well as fit multiple components, albeit tied to the same redshift.

We fit the full spectrum using MSAEXP, adopting Gaussian profiles for emission lines and a three-segment cubic spline to model the continuum. This minimal spline structure, appropriate given the high average S/N of GLIMPSE-17775 ($\gtrsim$30), helps prevent overfitting, particularly of features that may be slightly offset in wavelength/velocity space from the average redshift. Emission line positions are fixed; narrow components are allowed FWHM between 150–800 km s^{-1}, and permitted transitions may include a broad component (800–5000 km s^{-1}).

This yields a redshift of $z_{\rm spec} = 3.5010 \pm 0.0001$. However, several strong lines exhibit significant pixel-level offsets of 100–200 km s^{-1} relative to this value. These discrepancies are statistically robust and appear in both stacked and individual spectra, suggesting that the derived redshift reflects a weighted average dominated by high-S/N lines. To properly assess velocity structure, a consistent systemic redshift is required. This will be explored in the following sections.

Using the updated redshift alongside the strong-lensing model of AS1063 (Zitrin et al. 2015) and L. Furtak et al. (in prep.), we recalculate the lensing magnification to be $\mu = 2.04 \pm 0.21$, consistent with previous estimates based on $z_{\rm phot}$. With redshift and magnification now fixed, we turn to a deeper analysis of the emission line properties.

3.2. *Line Identification*

Beyond velocity offsets, the initial MSAEXP fit highlights several notable features. Broad hydrogen lines, which are ubiquitous in LRDs (e.g. Hviding et al. 2025; Matthee et al. 2023; Kocevski et al. 2023; Kokorev et al. 2023; Furtak et al. 2024; Taylor et al. 2025; de Graaff et al. 2025b; Naidu et al. 2025), are strongly favored across the Balmer and Paschen series, with $\Delta\chi^2 > 10$. These include Hα and Pa10 through Paγ. Although Paβ falls near the edge of the detector, we nonetheless observe a prominent broad wing at its expected location (see Figure 1).

Broad components are also detected in several helium and oxygen lines: He I λ6680, He I λ7065, O I λ8448, He I λ10830, and O I λ11290. Notably, the He I λ10830 line shows a classic P-Cygni profile with a clear blueshifted absorption trough. While Balmer absorption is becoming a familiar sight in LRDs (Matthee et al. 2023; Maiolino et al. 2023; Kocevski et al. 2024; de Graaff et al. 2025b; Naidu et al. 2025), helium absorption remains rare, with only a few published cases (e.g. Naidu et al. 2024; Wang et al. 2025; Juodžbalis et al. 2024) at high-z. Curiously this was also recently reported in local analogs of LRDs (Lin et al. 2025b).

The most striking feature is the detection of an extensive Fe II emission forest in the rest-NIR—at least 16 distinct features are identified by MSAEXP and highlighted in green in Figure 1. Previous detections of Fe II in LRDs have been mostly limited to rest-UV/optical wavelengths using low-resolution PRISM spectra (Labbe et al. 2024; Tripodi et al. 2025) and identified in local analogs (Lin et al. 2025b; Ji et al. 2025). Only recently have a few Fe II emitters been reported in medium- (D'Eugenio et al. 2025) and high-resolution spectra (Torralba et al. 2025). The richness of these lines in GLIMPSE-17775 hints at a dense, partially shielded gas phase, where processes such as Lyβ fluorescence and continuum pumping may be enhancing Fe II emission (Sigut & Pradhan 1998, 2003), offering a new diagnostic window into early AGN environments.

In summary, GLIMPSE-17775 exhibits an exceptionally rich and kinematically complex array of emission and absorption features. While the initial MSAEXP modeling provides a solid foundation for redshift estimation

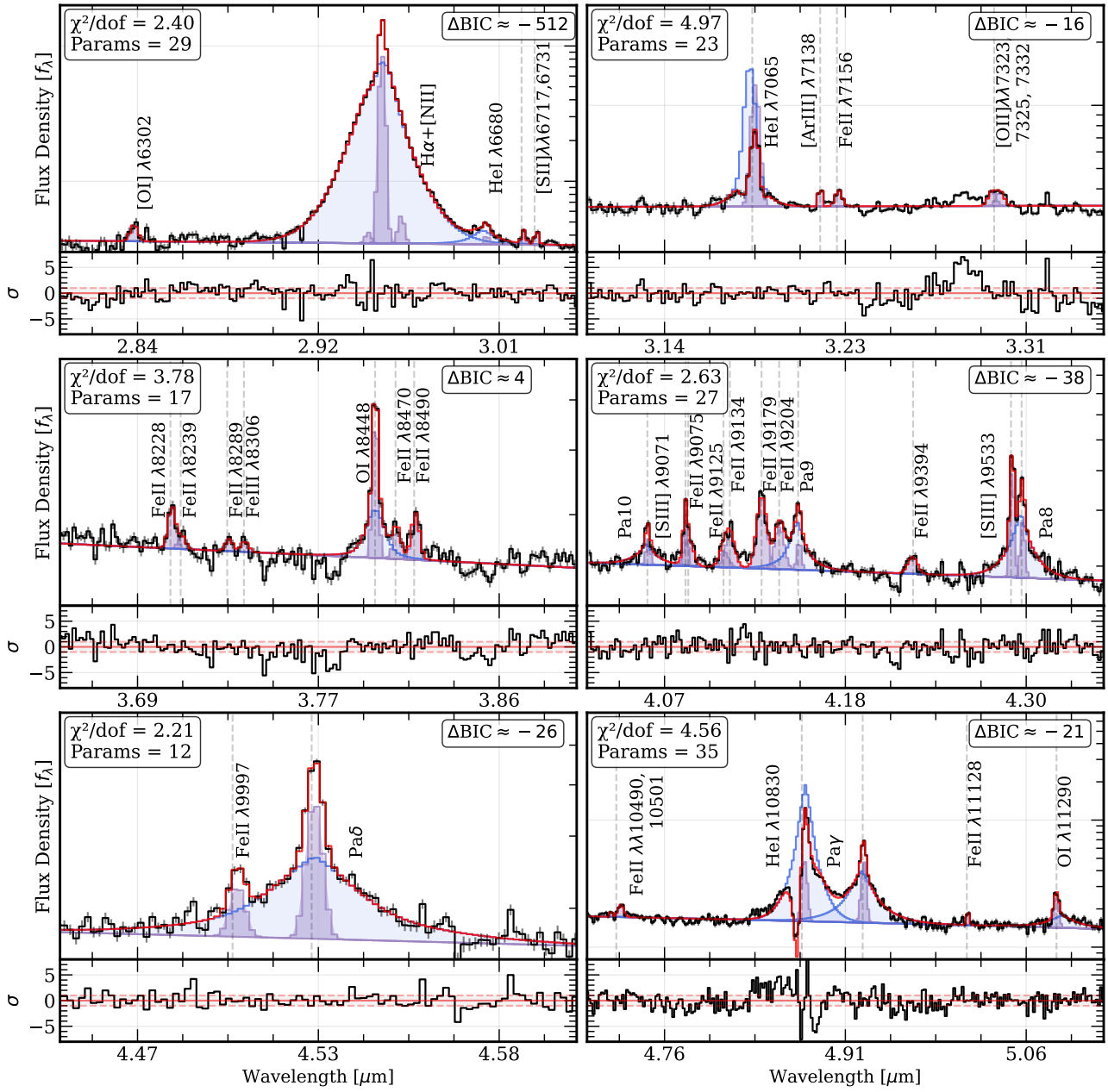

Figure 2. A staggering abundance of spectral lines in GLIMPSE-17775 at z=3.501. For each spectral window defined in Section 3.3, we show the data (black), the best-fit narrow and broad components (dark purple and blue), and the total best-fit model including the continuum (red). All broad components were fit with models allowing exponential wings. The ΔBIC between exponential and Gaussian fits is reported in the top right of each panel, negative number indicates a preference for an exponential profile. The lower panels display the uncertainty-weighted residuals for each fit.

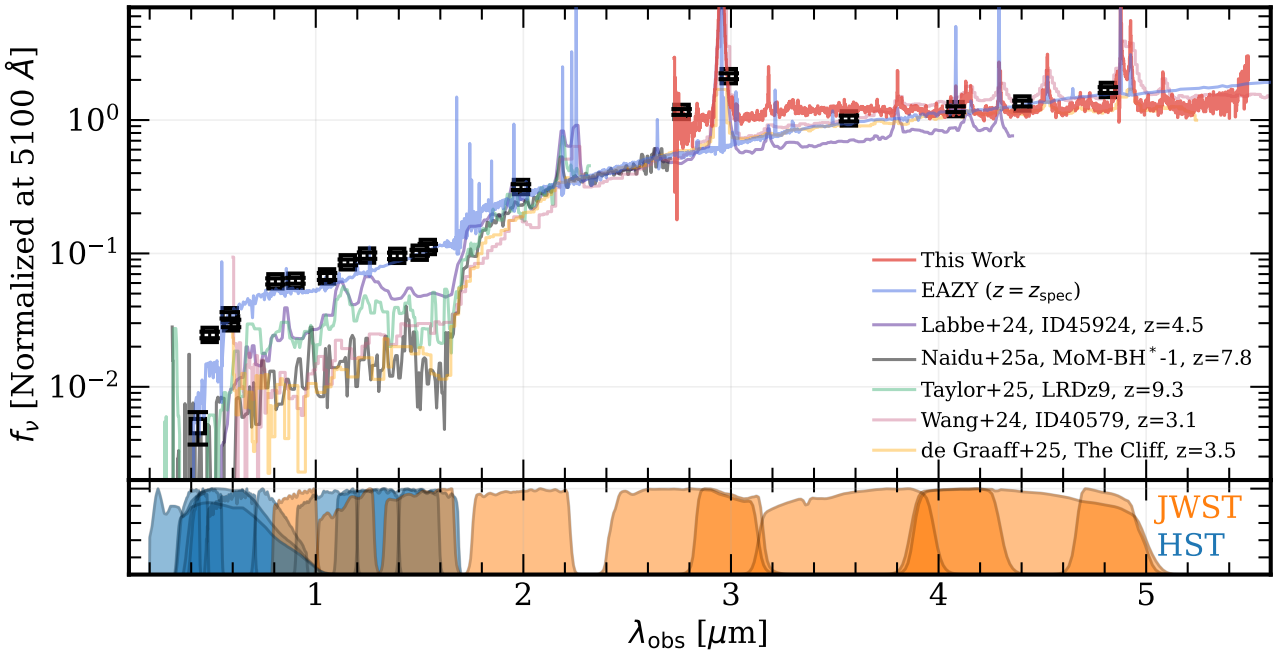

Figure 3. The diversity of Balmer breaks in LRDs. Black points show the *HST* and *JWST* GLIMPSE photometry of GLIMPSE-17775. Blue line shows best-fit EAZY SED fit to the photometry only, fixing the redshift to the z_{spec}. Maroon line show the combined and photometry-corrected G395M spectrum. While the red color in F200W-F277W is partially influenced by a bright Hα line, the Balmer break between F150W and F200W is still prominent. We further show spectra of various other LRDs (Labbe et al. 2024; Naidu et al. 2025; Taylor et al. 2025; Wang et al. 2024; de Graaff et al. 2025b), all shifted to $z = 3.501$ and normalized at 5100 Å. Finally, we show *HST* (blue) and *JWST* (orange) filter transmission curves below.

and line identification, it lacks the flexibility to capture the full diversity of line profiles in this high-S/N dataset. In the following sections, we peel back the spectral layers with increasing precision.

3.3. *Line Fitting*

The exceptional depth of the G395M spectrum for GLIMPSE-17775 enables detailed modeling of both multiple kinematic components and potential velocity offsets between line species. Unless noted otherwise, each line is fit with a single Gaussian narrow component (FWHM = 100–800 km s^{-1}). For permitted lines flagged by MSAEXP as potentially broad, we model the core with a Gaussian convolved with an exponential tail (Rusakov et al. 2025), with FWHM allowed between 500–5000 km s^{-1}. The degree of the convolution, i.e. the exponential "strength" is allowed to vary freely, however for every broad line we also perform a fit with that parameter fixed to zero (i.e. pure Gaussian) and compare it to our free fit. Line centers are allowed to vary independently, unless otherwise specified.

Absorption lines are modeled using a standard attenuation law with optical depth (τ_ν) as a free parameter (see Juodžbalis et al. 2024). Widths and redshifts (for both narrow and broad components) are typically free, with redshift limited to ± 0.1 from the MSAEXP value. Local continua are fit using first-order polynomials.

All of the individual model components are first initialized and co-added on an oversampled wavelength grid. To take into account the wavelength dependent resolution of the grating, we interpolate our model onto a variable step grid while making sure that the total integrated flux is preserved. Further, we increase the nominal spectral resolution by a factor of 1.7, as it has been shown that the spectral resolution for a point-like source falling within a shutter is higher than that of a uniformly illuminated slitlet (de Graaff et al. 2023). Fitting uses nonlinear χ^2 minimization with uncertainties being derived from multivariate resampling of the covariance matrix.

Given the complexity, the spectrum is divided into six windows grouped by line species or proximity (see Figure 2). Below we describe assumptions per window. Final fluxes and equivalent widths of the narrow and broad lines are listed in Table 2 and Table 3, respectively, while kinematics are reported in Table 4 and Table 5. We show detailed line fits in Figure 2.

3.3.1. *Hα complex*

Hα is modeled with independent narrow, broad, and absorption components. [O I] λ6302 and He I λ6680 are modeled with narrow and broad profiles. [N II] lines are fixed at a 1:3 ratio and share kinematics; [S II] lines have independent amplitudes but tied velocities and widths.

We find that broad Hα and He I λ6680 are strongly favored to have exponential wings (ΔBIC ~ -500), yielding FWHM ~ 1000 km s^{-1}—significantly narrower than the ~ 3000 km s^{-1} derived from pure Gaussians. Although no distinct Hα absorption component is explicitly detected, likely due to insufficient resolution, the overall asymmetry of the line is best reproduced when a weak, blueshifted absorber is included in the fit. This may indicate subtle self-absorption or partial obscuration within the dense cocoon. We return to the implications of this profile shape later.

3.3.2. *He* I λ7065

The He I λ7065 line shows a prominent blueshifted absorption component. We fit it with narrow, broad, and absorption profiles. The rest of the lines which include [Ar III] λ7138, Fe II λ7156, and the [O II] triplet ($\lambda\lambda$7323, 7325, 7332) are modeled as independent narrow lines.

He I λ7065 shows a strong preference for exponential wings (ΔBIC ~ -16) with FWHM $= 473 \pm 116$ km s^{-1}. A residual bump spanning from $\sim \lambda$7290–7320 is likely a combination of multiple Fe II, such as 7290, 7308 and potentially Fe III λ7319.65 lines. Curiously the latter line is often labeled as "hazy" in various emission line libraries (e.g. Kramida et al. 2024), which has an undefined shape as a result of pressure broadening or scattering in a very dense gas.

3.3.3. *O* I λ8448 *and Iron Lines*

In this part of the spectrum the O I λ8448 is fit with narrow and broad components. All of the iron lines, which include Fe II $\lambda\lambda$8228, 8239, 8289, 8470, 8490 as well as Fe III λ8306, are fit as narrow lines with shared kinematics. O I components are fit independently.

We find that the broad O I component is best described by a standard Gaussian profile, with a stronger statistical preference over exponential wings (ΔBIC $\sim$ 4). However, we caution that a trough at $\sim$3.77 μm, likely an artifact, may affect the reliability of the fit in this region

3.3.4. *Iron Forest and Paschen Lines*

This spectral region is among the most complex, due to the dense clustering of emission features. The Paschen lines Pa10–Pa8 are modeled with narrow and broad components. To reduce the number of free parameters, we tie all narrow Paschen components together kinematically, and do the same for the broad components. Fe II $\lambda\lambda$9075, 9125, 9134, 9179, 9204, 9394 are fit with shared centroid and width. [S III] lines are fit independently.

The [S III] λ9071 is used to define the systemic redshift: $z = 3.50102 \pm 0.00019$. This is done because the forbidden lines, such as [S III] or [O III], have lower critical densities, incompatible with the dense gas envelopes that gives rise to other line we observe. These lines may instead come from the host galaxy itself (e.g. Maiolino et al. 2023) and thus we choose this line to define the overall redshift of the system to measure all the offsets relative to it. All velocity offsets discussed in the subsequent sections are computed relative to this reference frame. The Paschen lines show strong preference for exponential wings (ΔBIC ~ -38), with FWHM $= 766 \pm 202$ km s^{-1}—narrower than Hα, but consistent within 2σ.

3.3.5. *Pa*δ

The Fe II λ9997 and Paδ complex is modeled with an independent narrow component for Fe II and both narrow and broad components for Paδ. There is no evidence for absorption. Exponential wings are again preferred (ΔBIC ~ -26). The resulting FWHM of 1672 ± 458 km s^{-1} is notably larger than that of both higher-order Paschen lines and Hα, though still consistent with the latter within 2σ.

3.3.6. *He* I λ10830 *and Pa*γ

The final window contains a complicated blend of broad He I λ10830 and Paγ lines, with a clear blueshifted absorption in the former. We fit a three component (narrow, broad and absorption) to He Iλ10830 and narrow+broad component to Paγ, keeping everything kinematically independent. We fit narrow Fe II at 10490, 10501 and 11128 Å with fixed redshift and line width. Finally the O I λ11290 is fit with independent narrow and broad component. Exponential wings are again preferred over pure Gaussian profile.

4. DATA ANALYSIS

4.1. *Morphology*

LRDs are unresolved in the rest-optical by definition, with measured sizes consistent with the PSF HWHM ($\lesssim 0\farcs07$ in F444W), and in some cases even smaller when dithers align favorably (e.g. Labbé et al. 2023b). Gravitational lensing can further push constraints on their intrinsic sizes to $\lesssim 100$ pc (Furtak et al. 2024).

In the rest-UV, however, a more complex picture is emerging. Several studies have now reported faint, extended, asymmetric components adjacent to the compact core (Labbe et al. 2024; Kokorev et al. 2024b;

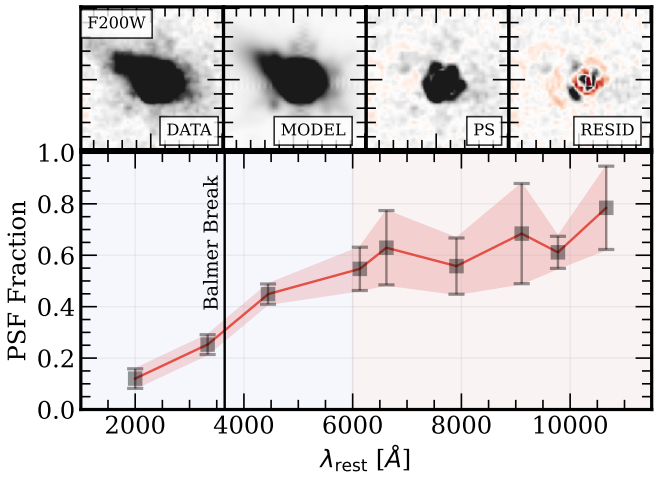

Figure 4. Top: Two-component Sérsic + point-source fit to the F200W morphology of GLIMPSE-17775. Panels show, from left to right, the data, best-fit model, model with the extended component removed, and residuals. **Bottom:** Fractional point-source contribution versus rest-frame wavelength. Shaded regions mark SW (blue) and LW (red) detectors, where the lower resolution of LW filters hinders reliable two-component decomposition.

.

Table 1. Source Properties.

Parameter†	GLIMPSE-17775
ID	17775
RA [deg]	342.20080
Dec [deg]	-44.54366
$z_{\rm phot}$ (EAZY)	4.2 ± 0.1
$z_{\rm spec}$ ([S III] λ9071)	3.50102 ± 0.00019
μ	2.04 ± 0.21
$M_{\rm UV}$ [AB mag]	-17.27 ± 0.05
$r_{\rm eff,UV}$ [pc]	1000±200
$r_{\rm eff,opt}$ [pc]	< 300
β	-0.69±0.12
$\log_{10}(M_{\rm BH}/M_\odot)$	6.65±0.15
$L_{\rm bol}$ [erg/s]	$(1.06\pm0.14)\times10^{45}$
$\lambda_{\rm edd}$	1.86 ± 0.25
$\log_{10}(M_*/M_\odot)_{\rm M_{UV}}$	< 7.5
$A_{\rm V}$	0.1±0.3
$f_{\nu,4050\text{Å}}/f_{\nu,3670\text{Å}}$	2.02 ± 0.10

† Physical parameters are corrected for the lensing magnification.

Table 2. Fluxes† of narrow emission lines and their rest-frame equivalent widths.

Line	$\lambda_{\rm rest}$ [Å]	Flux [10^{-20} erg s^{-1} cm^{-2}]	EW$_0$ [Å]
Narrow Emission Lines			
O I	6302.0	54.0 ± 21.2	3.3 ± 1.2
[N II]	6549.0	25.6 ± 10.3	1.6 ± 0.7
Hα	6562.8	2622.9 ± 200.7	167.7 ± 12.8
[N II]	6584.0	77.1 ± 37.1	4.9 ± 1.6
He I	6680.0	14.7 ± 11.1	0.8 ± 0.7
[S II]	6717.0	22.2 ± 0.1	1.5 ± 0.7
[S II]	6731.0	21.4 ± 0.1	1.4 ± 0.5
He I	7065.0	461.7 ± 210.2	31.0 ± 12.2
[Ar III]	7138.0	12.6 ± 3.4	1.0 ± 0.3
Fe II	7156.0	26.2 ± 7.2	1.8 ± 0.2
[O II]	7323.0	26.0 ± 23.0	1.7 ± 1.5
[O II]	7325.0	16.9 ± 1.8	1.2 ± 0.1
[O II]	7332.0	26.2 ± 9.1	1.8 ± 0.6
Fe II	8228.0	23.7 ± 4.2	2.0 ± 0.3
Fe II	8239.0	7.2 ± 4.0	0.6 ± 0.3
Fe II	8289.0	6.3 ± 3.7	0.5 ± 0.3
Fe III	8306.0	5.7 ± 3.6	0.5 ± 0.3
O I	8448.0	67.6 ± 2.4	6.1 ± 1.3
Fe II	8470.0	16.2 ± 5.0	1.4 ± 0.4
Fe II	8490.0	26.7 ± 4.3	2.4 ± 0.4
Pa10	9015.0	16.5 ± 5.0	1.8 ± 0.5
[S III]	9071.0	27.2 ± 2.3	3.5 ± 0.3
Fe II	9075.0	30.0 ± 4.7	3.4 ± 0.5
Fe II	9125.0	16.8 ± 5.2	1.9 ± 0.6
Fe II	9134.0	36.9 ± 5.0	4.1 ± 0.6
Fe II	9179.0	95.0 ± 5.5	10.6 ± 0.6
Fe II	9204.0	50.1 ± 6.1	5.6 ± 0.7
Pa9	9229.0	19.4 ± 7.0	2.2 ± 0.8
Fe II	9394.0	17.3 ± 3.9	2.0 ± 0.5
[S III]	9533.0	84.7 ± 5.9	10.2 ± 0.7
Pa8	9545.0	44.8 ± 11.3	5.4 ± 1.4
Fe II	9997.0	29.5 ± 4.5	3.8 ± 0.6
Paδ	10049.0	104.2 ± 12.2	13.7 ± 1.7
Fe II	10490.0	8.0 ± 2.7	1.1 ± 0.4
Fe II	10501.0	24.4 ± 5.9	3.1 ± 0.8
He I	10830.0	163.0 ± 96.0	22.6 ± 13.3
Paγ	10938.0	146.3 ± 25.5	20.9 ± 3.8
Fe II	11128.0	12.3 ± 3.7	1.8 ± 0.6
O I	11290.0	49.2 ± 4.1	7.7 ± 2.3

† Not corrected for lensing magnification.

Table 3. Fluxes† of broad emission lines and their rest-frame equivalent widths.

Line	$\lambda_{\rm rest}$	Flux	EW$_0$
	[Å]	[10^{-20} erg s^{-1} cm^{-2}]	[Å]
Broad Emission Lines			
Hα	6562.8	14803.5 ± 198.6	946.3 ± 15.6
He I	6680.0	144.6 ± 44.7	9.4 ± 2.9
He I	7065.0	824.2 ± 210.0	55.4 ± 15.1
Pa10	9015.0	53.7 ± 11.1	5.8 ± 1.3
Pa9	9229.0	119.0 ± 13.5	13.6 ± 1.5
Pa8	9545.0	191.2 ± 17.0	23.1 ± 2.1
Paδ	10049.0	370.6 ± 15.0	48.8 ± 2.3
He I	10830.0	2294.9 ± 212.6	318.8 ± 30.3
Paγ	10938.0	652.3 ± 14.0	92.9 ± 2.4
O I	8448.0	93.7 ± 7.9	8.4 ± 0.7
O I	11290.0	106.2 ± 63.9	16.6 ± 10.4

† Not corrected for lensing magnification.

Matthee et al. 2023; Rinaldi et al. 2025a,b), often suppressed by surface-brightness dimming. As shown in Figure 1, GLIMPSE-17775 likewise consists of two components out to F200W (rest ∼4000 Å), coincident with the Balmer break. Although we note that the break itself is much weaker than found in objects with very similar spectra (e.g. Wang et al. 2024) see Figure 3. At longer wavelengths, however, a point-source morphology takes over, consistent with a BH-dominated core. To quantify this transition, we model the NIRCam imaging using PYSERSIC (Pasha & Miller 2023) with a minimal configuration: a fixed-center point source plus a freely offset Sérsic profile. Normalizations, n, and $r_{\rm eff}$ are all allowed to vary, and uncertainties are drawn from the MCMC posteriors (e.g. Kokorev et al. 2024a).

Our fits show that the host galaxy dominates up to $\lambda_{\rm rest} \sim 4000$ Å, where the host and nucleus contribute roughly equally, beyond which the point source prevails to $\lambda_{\rm rest} \sim 1$ μm. Because the NIRCam LW detector has $\gtrsim$2× poorer resolution than the SW, a clean separation of host and nucleus in the rest-optical is impractical (e.g. see Whalen et al. 2025). Fortunately, F200W lies at the transition where both the resolution and flux ratio are favorable, so we use that band to illustrate our galaxy/LRD decomposition. We illustrate this in Figure 4, which also shows the increasing point-source fraction with wavelength, while acknowledging the uncertainties at longer wavelengths.

Table 4. Kinematic properties of narrow lines.

Line	$\lambda_{\rm rest}$	FWHM	Δv
	[Å]	[km s^{-1}]	[km s^{-1}]
Narrow Emission Lines			
[O I]	6300.3	455 ± 175	-101 ± 81
Hα	6562.8	304 ± 8	$+145 \pm 13$
[N II]	6583.4	347 ± 117	$+84 \pm 47$
[S II]	6716.4	232 ± 62	$+82 \pm 33$
[S II]	6731	232 ± 62	$+82 \pm 33$
He I	6678.2	87 ± 14	$+40 \pm 14$
He I	7065.2	408 ± 644	$+112 \pm 396$
[Ar III]	7135.8	89 ± 50	-26 ± 20
Fe II	7155.2	96 ± 50	$+15 \pm 15$
[O II]	7320.0	400 ± 120	-37 ± 72
Fe II	8228.0	290 ± 48	$+21 \pm 5$
Fe II	8239.0	290 ± 48	$+21 \pm 5$
Fe II	8289.0	290 ± 48	$+21 \pm 5$
Fe III	8306.0	290 ± 48	$+21 \pm 5$
O I	8446.4	235 ± 30	-43 ± 19
Fe II	8470.0	290 ± 48	$+21 \pm 5$
Fe II	8490.0	290 ± 48	$+21 \pm 5$
Pa10	9014.9	259 ± 36	-46 ± 19
[S III]	9071.0	230 ± 13	–
Fe II	9075.0	486 ± 24	-21 ± 17
Fe II	9125.0	486 ± 24	-21 ± 17
Fe II	9134.0	486 ± 24	-21 ± 17
Fe II	9179.0	486 ± 24	-21 ± 17
Fe II	9204.0	486 ± 24	-21 ± 17
Pa9	9229.0	259 ± 35	-46 ± 19
Fe II	9394.0	486 ± 24	-21 ± 17
Pa8	9545.6	259 ± 36	-46 ± 19
[S III]	9533	230 ± 13	$+23 \pm 13$
Fe II	9997.0	331 ± 55	$+90 \pm 25$
Paδ	10049.4	332 ± 22	$+21 \pm 15$
He I	10830.3	287 ± 46	$+112 \pm 26$
Paγ	10938.1	267 ± 25	$+26 \pm 17$
Fe II	10490.0	332 ± 96	$+44 \pm 43$
Fe II	10501.0	332 ± 96	$+44 \pm 43$
Fe II	11128.0	153 ± 116	$+37 \pm 30$
O I	11290.0	260 ± 58	-33 ± 24

Velocity offsets (Δv) calculated relative to [S III] λ9071 at $z = 3.50102$.

Table 5. Kinematic properties of broad and absorption lines.

Line	$\lambda_{\rm rest}$ [Å]	FWHM [km s^{-1}]	Δv [km s^{-1}]
Broad Emission Lines			
Hα	6562.8	1024 ± 21	-7 ± 16
He I	6678.2	1041 ± 792	-137 ± 151
He I	7065.2	473 ± 116	-136 ± 82
O I	8446.4	562 ± 331	$+39 \pm 80$
Pa10	9014.9	766 ± 202	-155 ± 39
Pa9	9229.0	766 ± 202	-155 ± 39
Pa8	9545.6	766 ± 202	-155 ± 39
Paδ	10049.4	1672 ± 458	$+23 \pm 44$
He I	10830.3	536 ± 45	$+154 \pm 22$
Paγ	10938.1	1035 ± 322	-75 ± 31
O I	11287.0	1188 ± 1099	$+245 \pm 214$
Absorption Lines			
Hα	6562.8	1000 ± 123	-200 ± 32
He I	7065.2	587 ± 1024	-52 ± 83
He I	10830.3	794 ± 21	$+45 \pm 22$

Velocity offsets (Δv) calculated relative to [S III] λ9071 at $z = 3.50102$.

After applying the lensing correction, we find that the extended component that dominates the UV light has a radius of $r_{\rm eff} \sim 1000$ pc, while the actual compact LRD, dominant in rest-optical, is fully consistent with the PSF and $r_{\rm eff} < 300$ pc.

4.2. *Dust Attenuation*

The ratio between observed emission line fluxes is commonly used to estimate dust extinction. For LRDs, this has typically been achieved through the Balmer decrement, provided that multiple Balmer lines are available. In our case, only Hα is detected. While the Paschen series, of which five lines are observed, could, in principle, be used to estimate extinction, the likely presence of stratified dense gas in LRDs (Naidu et al. 2025; de Graaff et al. 2025b) implies that the intrinsic line ratios may deviate significantly from standard Case B recombination expectations (Chang et al. 2025). Further, at the wavelengths of the Paschen series, the attenuation curves are practically flat (e.g. Calzetti et al. 2000), small offsets of the Case B ratios will a significant effect on the derived dust attenuation, but in return require extreme precision on measured line fluxes to be meaningful. Our uncertainties on e.g. Paγ/Paδ are small, roughly 10-15 %, this still leads to an impractically high uncertainty on the $A_{\rm V}$. To circumvent this limitation, we instead employ the ratio between the permitted O I λ8448 and O I λ11290 lines. These transitions share a common energy level, and under the assumption of Bowen (Lyβ) Fluorescence, all transitions through the λ11290 transition also cascade through the λ8448. This makes their intrinsic intensity set solely by the ratio of the inverse of their wavelengths

To ensure we are comparing the same physical gas component, we isolate the narrow emission peaks in both transitions, which show consistent widths of FWHM $\sim$ 250 km s^{-1}. This similarity supports the use of their flux ratio as a dust probe. We adopt the SMC attenuation curve (Gordon et al. 2003), widely used for high-redshift galaxies and reddened AGN (Capak et al. 2015; Reddy et al. 2015, 2018; Hopkins et al. 2004; Kokorev et al. 2023; Taylor et al. 2025). Assuming an intrinsic ratio of $(8448/11290)_{\rm int} = 1.336$ (Osterbrock 1989), we infer $A_V = 0.1 \pm 0.3$ mag, consistent with negligible extinction. Despite this, the optical continuum slope is red (βopt ~ 0.35), indicating that the continuum shape is dominated by the intrinsic SED of the dense cocoon rather than dust reddening.

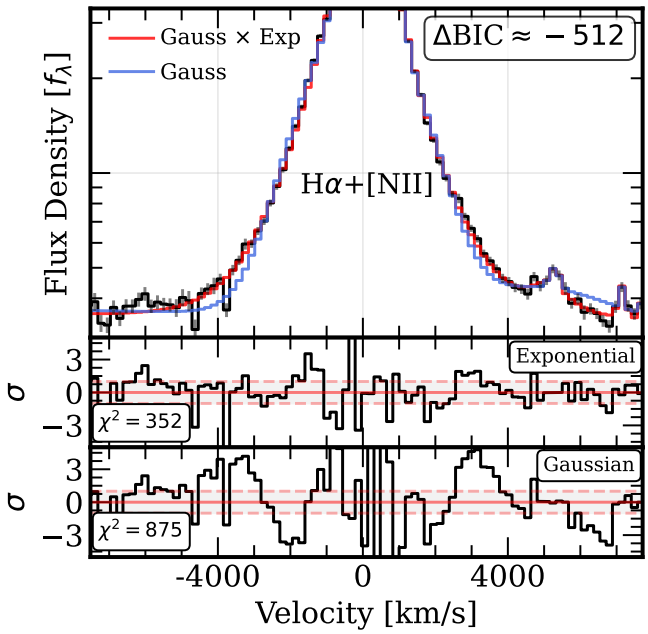

Figure 5. Exponential wings are required. Comparison of a Gaussian×Exponential model (red) and a single Gaussian profile (blue) for Hα. Uncertainties are shown with vertical lines in each spectral bin, albeit are too small to be visible. The exponential model provides a far superior fit, with smoother residuals and a strongly preferred ΔBIC, highlighting the necessity of exponential wings to capture the broad-line shape.

5. LINE PROPERTIES

Our fitting procedure yields over forty emission/absorption features, most of them are detected at a high (S/N> 3) significance. With all the pieces in place, we now would like to comment of the line profiles, kinematics as well as the specific line species that we find.

5.1. *Exponential Wings*

As already noted throughout Section 4, and further highlighted in Figure 2, all of the permitted lines, with the exception of O Iλ8448 which is likely impacted by data quality issues, in the spectrum are better fit when the broad line is convolved with an exponential profile. The statistical preference for this (as measured by the ΔBIC) being especially overwhelming for our brightest line - Hα. To further demonstrate this, and compare this fit to a more standard - Gaussian only approach, we show both of the models in Figure 5. If the broad line were to be only fit with a Gaussian profile, large portions of the line appear to be under-fit at a $\gtrsim 3\ \sigma$ significance level, while a model that includes exponential wings shows a much smoother, albeit not perfect, residual plot.

This strong preference for exponential wings is consistent with expectations from electron scattering in dense, ionized gas. Unlike Gaussian profiles, which would arise from Doppler broadening due to thermal and bulk motions around the SMBH, exponential profiles would only arise in environments dominated by electron scattering (e.g., Rusakov et al. 2025; Chang et al. 2025). The absence of strong broadening in the forbidden (e.g. [S II], [S III] and [N II]) lines already hints that the densities where these electron scattered profiles originate must already exceed multiple times that the critical density of those transitions ($n_e > 10^6$). Combined with the fact that these broad profiles are non-Gaussian in shape, the likely volume and column densities are likely to be even higher, at $n_e = 10^8$ cm^{-3} and $N_e \sim 10^{24}$ cm^{-2}, respectively, as suggested by both Rusakov et al. (2025) and Inayoshi & Maiolino (2025).

It is important to note that such detailed profile decomposition is only possible due to the exceptionally high S/N per pixel achieved in the line wings of our NIRSpec/G395M spectrum. As emphasized in Rusakov et al. (2025), these features would be impossible to distinguish with shallower data or lower-resolution modes such as NIRSpec/PRISM or even G395M exposures lacking comparable depth.

5.2. *Line Profiles*

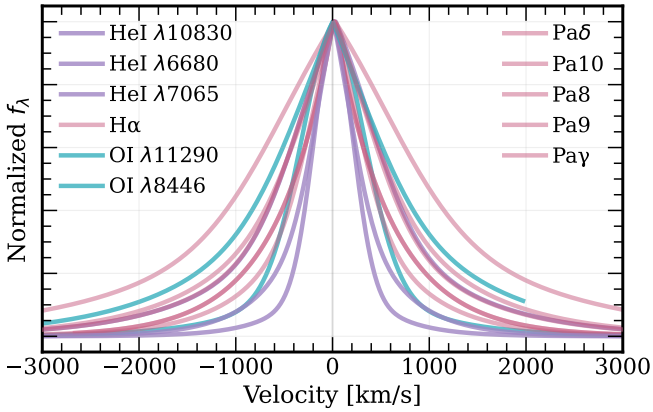

Figure 6. Best-fit profiles of all broad lines, oversampled and shifted to a common center. Hydrogen recombination (Hα and Paschen series) and O I lines show largely similar widths, consistent with their coupling through charge exchange. By contrast, He I lines are systematically narrower, likely reflecting their distinct metastable triplet physics and formation in a less dense, outer region.

Further, in Figure 6 we compare the best-fit models for all broad lines. As noted previously, with the exception of O I λ8448, every broad line is better described by exponential wings, resulting in very similar overall line shapes. The main differences arise in their widths. Despite some fits having sizable uncertainties, a trend emerges across line species. Hydrogen recombination lines (with the exception of Paδ) and O I transitions consistently show comparable FWHM values of $\sim$800 km s^{-1}. This agreement is not coincidental. Neutral oxygen and ionized hydrogen have nearly identical ionization potentials, enabling rapid charge-exchange coupling between $O^+ + H^0 \rightleftharpoons O^0 + H^+$ (Osterbrock & Ferland 2006). This continual electron exchange tightly locks the spatial distribution, ionization state, and kinematics of neutral oxygen to ionized hydrogen (and vice versa), so their broad-line profiles are naturally expected to track one another. The observed similarity therefore provides an important consistency check, reinforcing that the O I emission originates in the same dense, ionized gas as the hydrogen recombination lines. In contrast, the Fe II lines exhibit significantly narrower widths, matching the narrow cores of the permitted transitions rather than their exponential wings. This implies that the Fe II emission arises in a cooler, less turbulent zone exterior to the scattering-dominated region, but still closely coupled to the AGN continuum source.

By contrast, He I emission is systematically narrower. He I lines such as λ7065 and λ10830 do not couple to hydrogen via charge exchange, and their lower metastable level (2^3S) has distinct population physics, being fed by

both collisional and recombination pathways. Further, one has to take into account the radiative transfer effects, which make it possible to radiatively excite metastable ground state electrons. As a result, He I emission may arise from a somewhat different spatial or kinematic region than H and O. We return to this point in more detail below.

Taken together, the similar FWHM of hydrogen and oxygen broad-line profiles, combined with the near-universal exponential wings seen across all permitted transitions, strongly suggests that the line shapes are set by a common, line-independent scattering kernel rather than by transition-specific processes. Electron (Thomson) scattering in a dense, ionized cocoon provides a natural explanation: it produces exponential wings of nearly identical form across species, with widths set primarily by the electron temperature and column density (typically $\sim 10^{24}$ cm^{-2}), and leaves only secondary variations from species-specific excitation or optical depth effects (e.g. Chang et al. 2025; Rusakov et al. 2025). In this framework, the narrower He I lines reflect stratification within the cocoon, where He I emission arises from an outer region that has a lower density temperature or column density portion of the object, while the bulk hydrogen and oxygen emission share a common kinematic imprint within an inner - denser region.

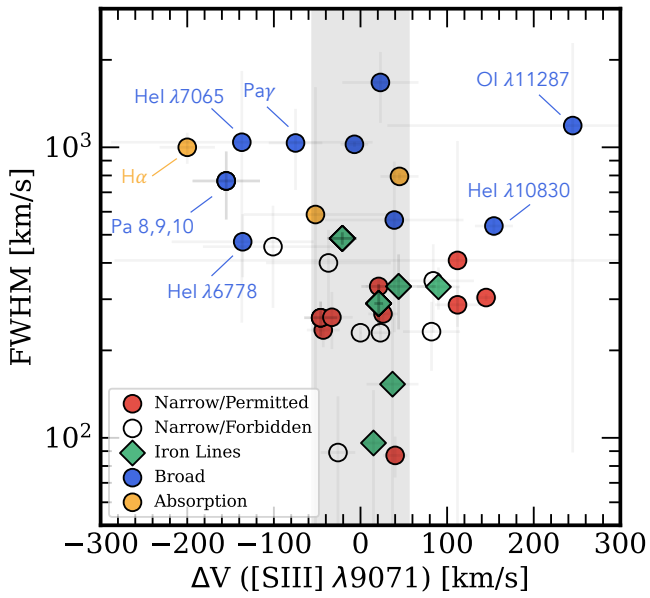

Figure 7. Velocity offsets (relative to [S III]λ9071) and FWHM for all detected lines. Narrow permitted lines are shown as maroon circles (open for forbidden), broad lines in blue, absorption in gold, and Fe II lines as green diamonds. The shaded band marks the velocity uncertainty set by the median spectral resolution. Narrow lines align closely with the systemic redshift, while absorption features show moderate blueshifts of ~ 150 km s^{-1}.

5.3. *Line Kinematics*

Before we proceed to discussing individual features in more detail, we would like to comment on the systematic velocity offsets between various line species in the spectrum on GLIMPSE-17775. As we mentioned before, we choose the redshift of the narrow forbidden [S III] λ9701 as the systemic one, due to it being relatively bright and isolated. We place all velocity offsets in context, by plotting all values from Table 4 and Table 5 in Figure 7.

While every fit formally yields a centroid, the significance of any offset is constrained by the spectral resolution and S/N of the data. To gauge which velocity shifts are meaningful, we adopt a conservative uncertainty of $\Delta V \sim \mathrm{med}(R)/5$, with $R = \lambda/\Delta\lambda$. This corresponds to ∼60 km s^{-1}, below which offsets are unlikely to be statistically significant.

Qualitatively, we do not find systematic shifts of either permitted or forbidden narrow lines relative to the systemic redshift. Iron lines also appear consistent with the systemic velocity. In contrast, the permitted broad lines, together with their associated absorption components, show a consistent blueshift of order ∼100 km s^{-1}.

Such blueshifts are commonly interpreted as signatures of outflowing gas in the broad-line region, where scattering and absorption occur preferentially along outflowing sight-lines. In the context of GLIMPSE-17775, this modest but systematic offset strengthens the case for a stratified cocoon, while the narrow lines trace gas in the outer regions at systemic velocity, the broad-line region and absorbing layers appear to be participating in bulk outflows. Confirming the detailed velocity structure, however, will require higher-resolution follow-up with the NIRSpec H-gratings (e.g. see Saldana-Lopez et al. 2025; Torralba et al. 2025).

5.4. *Hydrogen Absorption Lines*

Although no strong hydrogen absorption lines are explicitly detected, the Hα profile (Figure 2) shows a noticeable asymmetry, with suppressed flux on the blue side of the line. This feature is best modeled by a blueshifted (~ -200 km s^{-1}) absorption component, as already noted in Section 4. Similar non-resonant absorption signatures (e.g., Balmer lines) are now routinely observed in LRDs across a wide range of redshifts (e.g. Greene et al. 2024; Lin et al. 2024; Labbe et al. 2024; Taylor et al. 2025; Kokorev et al. 2024b). The presence of such absorption implies high gas densities of order $n \sim 10^9$ cm^{-3} (Inayoshi & Maiolino 2025; Hall 2007). Interestingly, only atoms in the $n = 2$ state appear significantly populated, as we detect no evidence

for Paschen absorption in any of the five lines present in our spectrum. This is also not an instrumental effect of the M-grating, as we clearly see an absorption feature in He I λ10830, but not the immediately adjacent Paγ. This indicates that $n = 3$ state is comparatively underpopulated.

Another key manifestation of the same physical mechanism is the Balmer break, corresponding to the $n = \infty \rightarrow n = 2$ transition limit. A prominent break is common in many LRD spectra (Setton et al. 2024), though not ubiquitous (e.g. Kokorev et al. 2023; Tripodi et al. 2025). While our spectral coverage does not extend to the Balmer limit itself, we observe a discontinuity of $\sim$1 mag between the F200W and F150W filters. Due to the F200W coverage of the SED, this flux jump cannot be attributed to line boosting from Hβ and the [O III] doublet. Adopting the break parametrization of Naidu et al. (2025) we use our best-fit SED and measure $f_{\nu,4050\text{Å}}/f_{\nu,3670\text{Å}} = 2.02 \pm 0.10$. Although weaker than the extreme values ($\sim 4-7$) reported for LRDz9 (Taylor et al. 2025), MoM BH*-1 (Naidu et al. 2025), or "the Cliff" (de Graaff et al. 2025b), this value lies close to the maximum achievable by evolved stellar populations (Wang et al. 2024; Labbe et al. 2024).

Taken together, the presence of asymmetry in the Hα profile, likely caused by blueshifted Balmer absorption, and a Balmer break adds to the evidence, complementing the exponential line wings, that the emission in GLIMPSE-17775 arises from a dense, ionized cocoon of gas. The lack of a detectable Paschen break is consistent with this picture, as high densities and optical depths result in Thomson scattering, but would also naturally wash out higher-order continuum edges (e.g. Wang et al. 2025). Assuming LTE, an extremely low ratio $n_3/n_2 \lesssim 0.01$ corresponds to an electron temperature of $T_e \sim 5000$ K or below, consistent with the warm, partially ionized gas expected in dense LRD cocoons.

We also observe moderately prominent and extremely prominent blueshifted absorption, respectively, in He I λ7065 and He I λ10830 the mechanism for this is similar, but not identical to the hydrogen lines. We also note the prominent blueshifted absorption seen in both He I λ7065 and He I λ10830. However, the physical mechanism driving these helium features differs fundamentally from that of the hydrogen lines, and we return to this in the following section.

5.5. *Helium Lines*

Both He I λ7065 and He I λ10830 show blueshifted ($\sim$70–80 km s^{-1} from the narrow-line center) absorption components with widths of $\sim$600–700 km s^{-1}. Unlike the Balmer series, helium transitions are resonantly scattered, so the arguments about $n = 2$ state abundances do not apply. Before addressing the absorption itself, it is useful to consider what the observed line strengths already tell us.

In the spectrum of GLIMPSE-17775 we detect three He I lines: λ6680, λ7065, and λ10830. These originate from different physical mechanisms. The λ6680 singlet line is produced via recombination or radiative pumping and is only weakly dependent on density. By contrast, λ7065 and λ10830 belong to the triplet system (along with λ3889, not covered by G395M), where the lower level is populated due to its very long lifetime. Electrons in this "ground state" can be can be collisionally or radiatively excited into higher energies and therefore the triplet lines strengths depend strongly on density and, to a lesser extent, temperature. As emphasized by Berg et al. (2025), He I λ10830 is the most sensitive density diagnostic among these transitions, followed by λ7065. The fact that both are much stronger than λ6680 indicates that the region where they form is very dense. The prominence of λ10830 in particular already points to a high-density environment with a temperature $T \gtrsim 10^4$ K. Further, the broad λ6680 has a noticeably higher FWHM compared to the triplet lines, but is consistent with hydrogen recombination lines. Which, again, makes sense since both originate from the same mechanism.

So what about absorption? Well, it turns out that its presence further reinforces this picture. The lower level (2^3S) of the triplet system is a metastable, long-lived state that effectively acts as a ground state in dense or partially ionized gas. As a result, photons from the 2^3P $\rightarrow$ 2^3S transition can be resonantly absorbed and re-emitted many times, analogous to Lyα or Mg II. This mechanism naturally produces strong absorption features when the He I column density is high. The fact that He I λ10830 not only dominates the helium spectrum in emission but also shows the deepest absorption in the entire spectrum provides compelling evidence for a dense, ionized cocoon of gas enshrouding GLIMPSE-17775.

5.6. *Oxygen Lines*

Above, we noted that O I λ8446 and λ11290 share very similar profiles with the hydrogen recombination lines. This is naturally expected because neutral oxygen is tightly coupled to hydrogen via charge exchange, which rapidly equilibrates the O/H ionization states in dense gas. When charge exchange is fast (high n_H), the O I/O II ratio tracks the H I/H II ratio, so the O I–emitting gas shares the same kinematics as the hydrogen recombination region (Draine 2011). The ob-

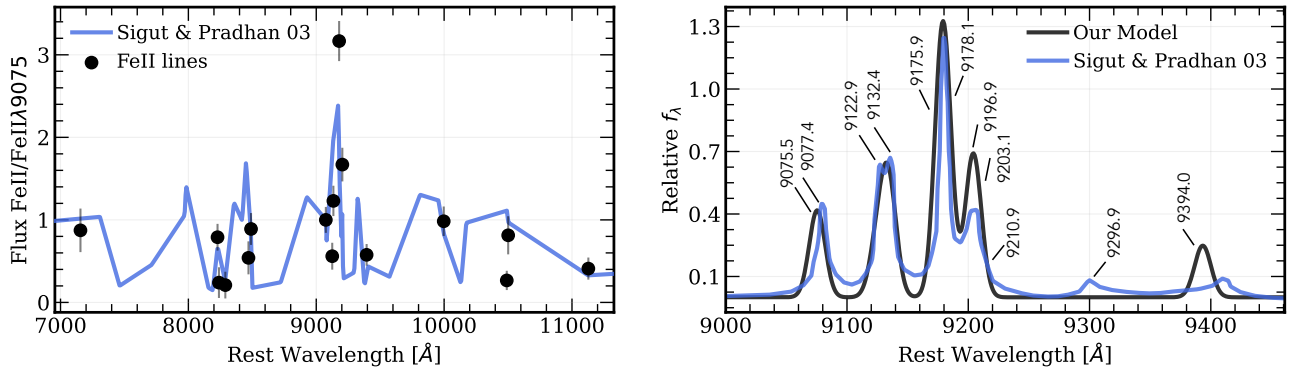

Figure 8. Lyα–pumped iron emission in GLIMPSE-17775. Left: Observed Fe II flux ratios (black points), normalized to Fe II λ9075, compared with predictions from Lyα fluorescence models of Sigut & Pradhan (2003) (blue). The close correspondence across ∼ 14 lines indicates a common excitation mechanism driven by Lyα pumping in dense, partially shielded gas. **Right:** Zoom-in on the λλ9000–9400 Å complex showing the remarkable agreement between the modeled continuum-subtracted Fe II spectrum (black) and the Sigut & Pradhan (2003) model (blue). We show air wavelengths of each Fe II line directly form Sigut & Pradhan, including the blended features. Together, these comparisons support an origin in the dense inner regions of the cocoon surrounding the accreting black hole.

served agreement in FWHM between H and O I lines is therefore an important consistency check that both species originate in the same dense, partially ionized phase.

A second, independent clue of high gas density and radiation field intensity comes from the excitation mechanism. The O I λ8446–λ11287 pair is the classic signature of Lyβ (Bowen) fluorescence: Lyβ pumps O I from the ground state and the ensuing cascade preferentially populates the levels that emit 1.129 μm that then cascade down through the 8446 Å line. In this channel, the line emissivity scales with both the neutral oxygen (or equivalently neutral hydrogen, via charge exchange) column and the local Lyβ radiation field, so producing strong O I fluorescence requires both a very bright Lyβ source and a dense neutral (or partially ionized) cocoon.

Further, we do not detect (5σ upper limit $< 12/[10^{-20}$ erg s^{-1}cm^{-2}]) any other of the permitted O I λ7774, λ7254, and λ7790 lines, and the [O I] λ6302/O I λ8446 ratio is weak. If collisional excitation or pure recombination dominated, these lines would be comparatively strong; their absence strongly favors Bowen fluorescence as the primary driver of the observed O I emission.

Finally, the velocity structure adds a natural stratification: hydrogen recombination and O I (fluorescent, charge-exchange coupled) share widths and profiles, while He I lines are systematically narrower. Since He I triplet transitions emerge from a metastable 2^3S level (with distinct, density-sensitive population pathways and resonant transfer), they likely trace a kinematically distinct layer within the same cocoon.

5.7. *Lyα Fluorescence in Iron Lines*

Permitted iron emission, primarily Fe II and Fe III (e.g. Labbe et al. 2024; Tripodi et al. 2025; Torralba et al. 2025), but in some cases extending to highly ionized species such as Fe VII (Tang et al. 2025; Lambrides et al. 2025) and Fe X (Furtak et al. 2024), has become a recurring feature in LRD spectra. In GLIMPSE-17775, the spectrum is exceptionally rich in near-infrared iron lines: we identify 16 Fe II and one Fe III transition. Understanding the origin of this emission is key to interpreting the dense gas environment in LRDs.

The physics of Fe II emission has long been a challenge for BLR photoionization models (Joly 1993). Thick, high-column density ($\sim 10^{25}$ cm^{-2}) gas at the edges of the accretion disk has been invoked as a potential source (Joly 1987; Collin-Souffrin et al. 1988), where the scattering and absorption of the hard X-ray photons would ionize the gas. Similarly, this would also enhance the Balmer and Paschen line luminosities. Further, extensive theoretical work has shown that Lyα fluorescence is fundamental in reproducing the observed Fe II strengths (Sigut & Pradhan 1998, 2003). Lyα pumping not only boosts the UV and optical Fe II emission, but also predicts strong lines in the near-infrared.

This expectation aligns closely with our observations. In Figure 8, we compare our measured Fe II flux ratios (normalized to Fe II λ9075) against the Lyα-pumped model predictions of Sigut & Pradhan (2003). With the exception of Fe II λ9179, affected by blending with Fe II λ9204 and Pa9, we find remarkably good agreement across the suite of detected features. In particular, the dense forest of Fe II transitions spanning λλ9000–9200 Å (center-right panel in Figure 2) is reproduced almost exactly by the theoretical spectrum (cf. Fig. 11 in Sigut &

Pradhan 2003). We overlay the Sigut & Pradhan model directly on our continuum-subtracted fit in Figure 8, demonstrating that the observed Fe II emission is fully consistent with fluorescence in dense gas near the broad-line region. The implication is that the majority of the Fe II emission in GLIMPSE-17775 arises through Lyα pumping, directly tracing an extremely dense medium, ionized by an extremely luminous source - likely an accreting black hole. Given that the Fe II are somewhat narrower compared to other permitted features, it is likely that the emitting region is further from the BLR, something that has already been shown in a classic example of narrow Fe II emitter - I Zw 1 (Rudy et al. 2000; Marinello et al. 2016).

Together with the Balmer absorption, helium triplet features, and Bowen fluorescence in O I, the iron forest adds another piece of evidence that points to a dense cocoon enshrouding the black hole.

5.8. *Source Properties*

Based on the previous discussion, we now present the likely physical properties of the black hole and its host. The coexistence of broad permitted and narrow forbidden lines indicates, as in most LRDs (Hviding et al. 2025), that the broad components originate in an AGN broad-line region (BLR). Following Greene & Ho (2005), we derive $M_{\rm BH}$ from the luminosity and width of the broad Hα line, assuming the exponential-wing profile demonstrated in Figure 2 and Figure 5. With FWHMHα $= 1024 \pm 21$ km s^{-1}, negligible dust, and $\mu = 2.04$, we obtain $\log(M_{\rm BH}/M_\odot) = 6.65 \pm 0.15$, where the dominant uncertainty arises from the Greene & Ho calibration. A purely Gaussian fit, though statistically disfavored, would yield a FWHM three times larger and a black hole mass nearly a dex higher. Throughout this work we adopt the $M_{\rm BH}$ from the exponential model.

Further, by assuming that the bolometric luminosity ($L_{\rm bol}$) scales as $L_{\rm bol} = 130 \times L_{\rm H\alpha}$ (Richards et al. 2006), we find $L_{\rm bol} = (1.06 \pm 0.14) \times 10^{45}$ erg/s. Using our $M_{\rm BH}$ derived by assuming exponential wings, we then find that this object is accreting at a super-Eddington rate - $L_{\rm bol}/L_{\rm edd} = 1.86 \pm 0.25$. This is higher than the vast majority of LRDs at all redshifts (e.g. Taylor et al. 2025; Kokorev et al. 2023; Juodžbalis et al. 2024; Akins et al. 2025; Furtak et al. 2024; Maiolino et al. 2023; Kocevski et al. 2024), which are found to accrete at sub-Eddington rates. However recent works examining LRDs with extreme Balmer breaks derive accretion rates that exceed the Eddington limit (de Graaff et al. 2025b; Naidu et al. 2025; Lambrides et al. 2024).

A recent work examining multi-wavelength LRD data however has suggested that the bolometric luminosity emerges mostly from the rest-frame optical, with X-rays and radio contributions being largely subdominant (Greene et al. 2025). Given the suggested dominance of the optical light in LRDs, the much lower bolometric corrections ($\times 7-10$ lower) would potentially imply lower black hole masses and total bolometric luminosities (e.g. derived from Hα) than the standard (e.g Greene & Ho 2005) might suggest. This adjustment would lower both the inferred black hole masses and bolometric luminosities (e.g., those derived from Hα). However, because the two quantities scale together, the implied super-Eddington nature of GLIMPSE-17775 would remain unchanged, though the black hole mass could decrease to $\sim 10^{5.5}$–$10^{5.8}\,M_\odot$. A more detailed reassessment of bolometric corrections for LRDs is clearly warranted, but such an analysis lies beyond the scope of this work. For consistency with previous studies, we adopt the standard AGN bolometric corrections throughout, with all derived parameters listed in Table 1.

Finally, we estimate an upper limit on the stellar mass in GLIMPSE-17775. Previous studies have modeled LRDs using joint galaxy+AGN SED decomposition (e.g., Furtak et al. 2024; Kokorev et al. 2023), and more recently within the BH* framework have assumed that most of the rest–UV flux arises from the host galaxy (Taylor et al. 2025; Naidu et al. 2025). Our spatial decomposition (Figure 4) supports this assumption: the extended component contributes $> 80\%$ of the rest–UV light, implying that the bulk of the stellar mass resides in this resolved structure. Given this, we adopt a simple empirical approach using the $M_{\rm UV}$–M_* relation (e.g. Stark et al. 2009; Labbé et al. 2013) and obtain a conservative upper limit on the stellar mass of $M_* \lesssim 10^{7.5} M_\odot$. This in return gives us a BH-to-host mass ratio of $\lesssim 0.14$, which is significantly elevated from local expectations (Greene & Ho 2005), but is not as extreme as some other LRDs reported in the literature (Furtak et al. 2024; Kokorev et al. 2023; Maiolino et al. 2023).

6. DISCUSSION AND SUMMARY

6.1. *Dense and Ionized Gas Surrounding the AGN*

Our NIRSpec/G395M observations of GLIMPSE-17775 reveal a remarkably consistent picture: across independent tracers, the line emission requires an environment of extremely high density and partial ionization.

First, the broad permitted lines are universally better fit by exponential wings, a hallmark of electron scattering in gas with $n_{\rm e} \gtrsim 10^8$ cm^{-3} and column densities approaching $N_{\rm e} \sim 10^{24}$ cm^{-2}. Such profiles are not reproduced by Doppler broadening alone and point to an ionized scattering medium enveloping the source. The

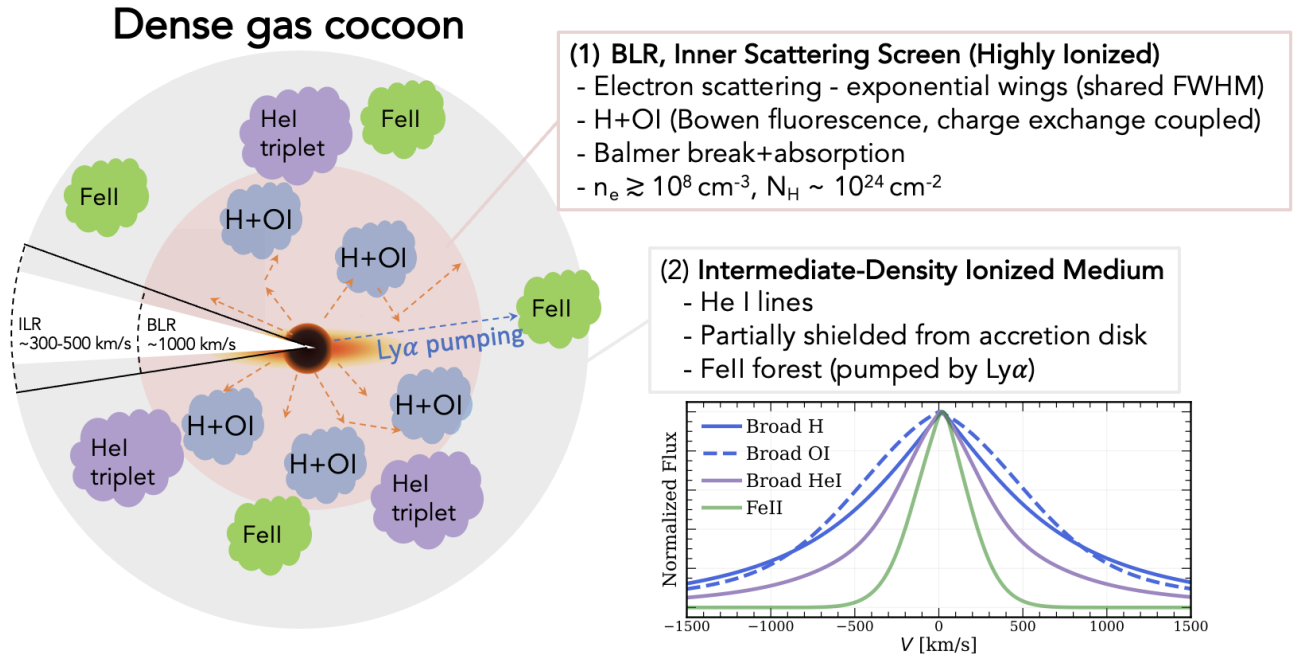

Figure 9. Physical picture of the dense cocoon around GLIMPSE-17775. The inner region (1) corresponds to the dense, highly ionized broad-line region where electron scattering (orange lines) produces exponential wings, H and O I share coupled kinematics (via charge exchange and Bowen fluorescence), and strong Balmer absorption/break signatures arise. The outer layer (2) represents an intermediate-density ionized medium, where He I triplet lines show resonant absorption from the metastable 2^3S level and Fe II emission is driven by Lyα fluorescence. Together, these zones form a stratified cocoon enshrouding the accreting black hole. Bottom right panel shows stacks line profiles of H, O I, He I and Fe II.

fact that hydrogen and O I lines share consistent FWHM values further anchors this interpretation, as charge exchange tightly couples neutral oxygen to the ionization and kinematics of hydrogen.

Second, the detection of blueshifted Balmer absorption and a significant Balmer break both require high $n = 2$ populations and densities $n \sim 10^9$ cm^{-3}. Helium transitions provide a complementary view: the triplet lines λ7065 and λ10830 are both strongly enhanced relative to the singlet states and show deep blueshifted absorption, consistent with resonant scattering from the metastable 2^3S level. Their systematically narrower widths compared to hydrogen and oxygen suggest stratification, with helium arising from denser, more compact layers of the cocoon.

Third, the O I λ8446–λ11290 pair confirms Lyβ fluorescence, requiring both a bright Lyβ radiation field and a dense reservoir of neutral gas. The absence of other permitted O I lines not fed by Lyβ strengthens this conclusion. Finally, the detection of 16 Fe II lines, forming an incredibly rich iron forest in this LRD, matches predictions from Lyα fluorescence models, again demanding an intense radiation field and very high densities.

Because the BLR is unresolved in essentially all AGN, broad-line widths are traditionally interpreted as virial tracers of the black hole potential. In GLIMPSE-17775, the virial story alone is insufficient: the issue is not how broad the lines are, but how they broaden. The profiles exhibit extended, nearly linear wings in velocity space that are incompatible with a Gaussian. Instead, the lines are systematically and significantly better described by a model consisting of a narrow Gaussian core (virial motion) plus exponential wings, the hallmark of Thomson scattering in a dense ionized medium. Thus, the line shape encodes both gravitational kinematics and radiative-transfer physics in the surrounding cocoon. Our schematic (Figure 9) summarizes this revised view: in LRDs, broad-line profiles are not set by dynamics alone, but by the scattering environment through which the photons escape.

Such conditions—high optical depths, large column densities, and evidence for radiation-dominated gas—are precisely those expected in super-Eddington accretion flows. In this regime, radiation pressure inflates the inner accretion structure, driving powerful winds and forming the very dense, partially ionized envelope we infer here. The low X-ray luminosities and weak radio emission commonly observed in LRDs (e.g., Akins et al. 2024; Ananna et al. 2024; Kokubo & Harikane 2024; Yue et al. 2024) are consis-

tent with this picture: the X-rays are likely absorbed or thermalized within the optically thick cocoon, while dust cannot survive in such an intense radiation field (e.g., Inayoshi & Maiolino 2025; Naidu et al. 2025; de Graaff et al. 2025b; Taylor et al. 2025; Lambrides et al. 2024). Thus, the spectroscopic signatures observed in GLIMPSE-17775—exponential wings, absorption features, and fluorescence-driven metal lines—fit naturally into a scenario where super-Eddington accretion onto a low-mass black hole powers the luminous yet heavily reprocessed emission.

Taken together, the exponential wings, Balmer and helium absorption, Bowen oxygen lines, and Lyα-pumped iron forest all converge on the same physical picture: GLIMPSE-17775 is enshrouded in a dense, partially ionized cocoon of gas.

6.2. *Final Remarks*

Using a combination of the intrinsically deepest NIRCam photometry and NIRSpec/G395M observations of the lensed AS1063 field, we present a detailed investigation of a little red dot at $z = 3.501$. The spectrum of GLIMPSE-17775 is exceptionally rich, with more than forty detected features, allowing us to probe the physical conditions of the gas with unprecedented detail. Multiple independent diagnostics converge on the presence of a dense, partially ionized cocoon heated by a powerful ionizing source.

Typical of other LRDs, GLIMPSE-17775 is extremely compact in the rest-optical ($r_{\rm eff} < 300$ pc) but exhibits more extended structure in the rest-UV ($r_{\rm eff} \sim 1000$ pc; Figure 1). It shows unmistakable AGN signatures through broad permitted lines (e.g., Greene et al. 2024; Kocevski et al. 2023; Kokorev et al. 2023; Furtak et al. 2024). The uniquely deep G395M spectrum further reveals clues to the physical origin of both its continuum and line-emission properties. We detect exponential broad-line wings, Balmer and helium absorption, Bowen–pumped O I, Fe II emission produced by Lyα fluorescence, and evidence for rapid, potentially super-Eddington growth.

Together, these diagnostics provide one of the clearest cases yet for the BH* "dense cocoon" scenario (Inayoshi & Maiolino 2025; Naidu et al. 2025; de Graaff et al. 2025b; Taylor et al. 2025). The same ingredients we observe—exponential broad wings, Balmer-break absorption, He I absorption, and rich Fe II and O I fluorescence—have been detected individually in several other bright LRDs with medium- and high-resolution spectroscopy (e.g. Torralba et al. 2025; D'Eugenio et al. 2025; Labbe et al. 2024; Furtak et al. 2024; Wang et al. 2025; Juodžbalis et al. 2024; Lambrides et al. 2025), suggesting that dense, optically thick gas may be a common feature of the population rather than an anomaly. What distinguishes GLIMPSE-17775 is that all signatures are captured simultaneously and at high S/N, allowing a self-consistent physical interpretation. If such cocoons are widespread, then super-Eddington accretion may be a typical pathway for black-hole growth in LRDs, especially among the most luminous systems. Establishing how these signatures vary with luminosity and redshift will be essential for determining whether dense cocoons represent a dominant mode of early black-hole assembly.

The convergence of five independent diagnostics—exponential scattering wings, Balmer-limit absorption, helium triplet physics, and two distinct fluorescence channels—leaves little doubt: GLIMPSE-17775 hosts a dense ($n \sim 10^{8-9}$ cm^{-3}), optically thick ($N_e \sim 10^{24}$ cm^{-2}) cocoon of partially ionized gas surrounding a super-Eddington accreting black hole. This represents some of the most direct and comprehensive spectroscopic evidence to date for the dense cocoon scenario in LRDs.

ACKNOWLEDGMENTS

The authors would like to acknowledge the National Institute of Standards and Technology (NIST) database of spectral lines (Kramida et al. 2024), which made identification of less-known emission features possible. VK, JC, SF, DB, LF, TH and JM acknowledge support from the University of Texas at Austin Cosmic Frontier Center. AZ acknowledges support by the Israel Science Foundation Grant No. 864/23. This work is based on observations made with the NASA/ESA/CSA *James Webb Space Telescope*, obtained at the Space Telescope Science Institute, which is operated by the Association of Universities for Research in Astronomy, Incorporated, under NASA contract NAS5-03127. The JWST data presented in this article were obtained from the Mikulski Archive for Space Telescopes (MAST) at the Space Telescope Science Institute. The specific observations analyzed can be accessed via doi: 10.17909/4byn-fe55 and doi: 10.17909/zq0c-8t87. These observations are associated with programs GO #3293 and DDT #9223.

Software: EAZY (Brammer et al. 2008), grizli (Brammer 2023), msaexp (Brammer 2022), photutils (Bradley et al. 2020), pysersic (Pasha & Miller 2023), sep (Barbary 2016), SExtractor (Bertin & Arnouts 1996)

Facilities: JWST, *HST*

REFERENCES

Akins, H. B., Casey, C. M., Lambrides, E., et al. 2024, arXiv e-prints, arXiv:2406.10341, doi: 10.48550/arXiv.2406.10341

Akins, H. B., Casey, C. M., Berg, D. A., et al. 2025, ApJL, 980, L29, doi: 10.3847/2041-8213/adab76

Ananna, T. T., Bogdán, Á., Kovács, O. E., Natarajan, P., & Hickox, R. C. 2024, ApJL, 969, L18, doi: 10.3847/2041-8213/ad5669

Arrabal Haro, P., Dickinson, M., Finkelstein, S. L., et al. 2023, Nature, 622, 707, doi: 10.1038/s41586-023-06521-7

Barbary, K. 2016, Journal of Open Source Software, 1, 58, doi: 10.21105/joss.00058

Barro, G., Perez-Gonzalez, P. G., Kocevski, D. D., et al. 2024, arXiv e-prints, arXiv:2412.01887, doi: 10.48550/arXiv.2412.01887

Berg, D. A., Sanders, R. L., Shapley, A. E., et al. 2025, arXiv e-prints, arXiv:2507.17057, doi: 10.48550/arXiv.2507.17057

Bertin, E., & Arnouts, S. 1996, A&AS, 117, 393, doi: 10.1051/aas:1996164

Boylan-Kolchin, M. 2023, Nature Astronomy, 7, 731, doi: 10.1038/s41550-023-01937-7

Bradley, L., Sipőcz, B., Robitaille, T., et al. 2020, astropy/photutils: 1.0.0, 1.0.0, Zenodo, doi: 10.5281/zenodo.4044744

Brammer, G. 2022, msaexp: NIRSpec analyis tools, 0.3, doi: 10.5281/zenodo.7299500

Brammer, G. 2023, grizli, 1.8.2, Zenodo, Zenodo, doi: 10.5281/zenodo.7712834

Brammer, G. B., van Dokkum, P. G., & Coppi, P. 2008, ApJ, 686, 1503, doi: 10.1086/591786

Calzetti, D., Armus, L., Bohlin, R. C., et al. 2000, ApJ, 533, 682, doi: 10.1086/308692

Capak, P. L., Carilli, C., Jones, G., et al. 2015, Nature, 522, 455, doi: 10.1038/nature14500

Casey, C. M., Akins, H. B., Kokorev, V., et al. 2024, arXiv e-prints, arXiv:2407.05094. https://arxiv.org/abs/2407.05094

Chabrier, G. 2003, PASP, 115, 763, doi: 10.1086/376392

Chang, S.-J., Gronke, M., Matthee, J., & Mason, C. 2025, arXiv e-prints, arXiv:2508.08768, doi: 10.48550/arXiv.2508.08768

Chemerynska, I., Atek, H., Furtak, L. J., et al. 2025, arXiv e-prints, arXiv:2509.24881, doi: 10.48550/arXiv.2509.24881

Collin-Souffrin, S., Hameury, J. M., & Joly, M. 1988, A&A, 205, 19

de Graaff, A., Rix, H.-W., Carniani, S., et al. 2023, arXiv e-prints, arXiv:2308.09742, doi: 10.48550/arXiv.2308.09742

de Graaff, A., Setton, D. J., Brammer, G., et al. 2024, arXiv e-prints, arXiv:2404.05683, doi: 10.48550/arXiv.2404.05683

de Graaff, A., Brammer, G., Weibel, A., et al. 2025a, A&A, 697, A189, doi: 10.1051/0004-6361/202452186

de Graaff, A., Rix, H.-W., Naidu, R. P., et al. 2025b, arXiv e-prints, arXiv:2503.16600, doi: 10.48550/arXiv.2503.16600

D'Eugenio, F., Nelson, E., Ji, X., et al. 2025, arXiv e-prints, arXiv:2510.00101, doi: 10.48550/arXiv.2510.00101

Draine, B. T. 2011, Physics of the Interstellar and Intergalactic Medium

Endsley, R., Chisholm, J., Stark, D. P., Topping, M. W., & Whitler, L. 2024, arXiv e-prints, arXiv:2410.01905, doi: 10.48550/arXiv.2410.01905

Fei, Q., Fujimoto, S., Naidu, R. P., et al. 2025, arXiv e-prints, arXiv:2509.20452, doi: 10.48550/arXiv.2509.20452

Fujimoto, S., Naidu, R. P., Chisholm, J., et al. 2025, arXiv e-prints, arXiv:2501.11678, doi: 10.48550/arXiv.2501.11678

Furtak, L. J., Labbé, I., Zitrin, A., et al. 2024, Nature, 628, 57, doi: 10.1038/s41586-024-07184-8

Gordon, K. D., Clayton, G. C., Misselt, K. A., Landolt, A. U., & Wolff, M. J. 2003, ApJ, 594, 279, doi: 10.1086/376774

Greene, J. E., & Ho, L. C. 2005, ApJ, 630, 122, doi: 10.1086/431897

Greene, J. E., Labbe, I., Goulding, A. D., et al. 2024, ApJ, 964, 39, doi: 10.3847/1538-4357/ad1e5f

Greene, J. E., Setton, D. J., Furtak, L. J., et al. 2025, arXiv e-prints, arXiv:2509.05434, doi: 10.48550/arXiv.2509.05434

Hall, P. B. 2007, AJ, 133, 1271, doi: 10.1086/511272

Hopkins, P. F., Strauss, M. A., Hall, P. B., et al. 2004, AJ, 128, 1112, doi: 10.1086/423291

Horne, K. 1986, PASP, 98, 609, doi: 10.1086/131801

Hviding, R. E., de Graaff, A., Miller, T. B., et al. 2025, arXiv e-prints, arXiv:2506.05459, doi: 10.48550/arXiv.2506.05459

Inayoshi, K., & Maiolino, R. 2025, ApJL, 980, L27, doi: 10.3847/2041-8213/adaebd

Ji, X., D'Eugenio, F., Juodžbalis, I., et al. 2025, arXiv e-prints, arXiv:2507.23774, doi: 10.48550/arXiv.2507.23774

Joly, M. 1987, A&A, 184, 33

—. 1993, Annales de Physique, 18, 241, doi: 10.1051/anphys:01993001803024100

Juodžbalis, I., Ji, X., Maiolino, R., et al. 2024, MNRAS, 535, 853, doi: 10.1093/mnras/stae2367

Kocevski, D. D., Onoue, M., Inayoshi, K., et al. 2023, arXiv e-prints, arXiv:2302.00012, doi: 10.48550/arXiv.2302.00012

Kocevski, D. D., Finkelstein, S. L., Barro, G., et al. 2024, arXiv e-prints, arXiv:2404.03576, doi: 10.48550/arXiv.2404.03576

Kokorev, V., Brammer, G., Fujimoto, S., et al. 2022, ApJS, 263, 38, doi: 10.3847/1538-4365/ac9909

Kokorev, V., Fujimoto, S., Labbe, I., et al. 2023, ApJL, 957, L7, doi: 10.3847/2041-8213/ad037a

Kokorev, V., Caputi, K. I., Greene, J. E., et al. 2024a, ApJ, 968, 38, doi: 10.3847/1538-4357/ad4265

Kokorev, V., Chisholm, J., Endsley, R., et al. 2024b, ApJ, 975, 178, doi: 10.3847/1538-4357/ad7d03

Kokorev, V., Atek, H., Chisholm, J., et al. 2025, ApJL, 983, L22, doi: 10.3847/2041-8213/adc458

Kokubo, M., & Harikane, Y. 2024, arXiv e-prints, arXiv:2407.04777, doi: 10.48550/arXiv.2407.04777

Korber, D., Chemerynska, I., Furtak, L. J., et al. 2025, arXiv e-prints, arXiv:2510.04771, doi: 10.48550/arXiv.2510.04771

Kramida, A., Yu. Ralchenko, Reader, J., & and NIST ASD Team. 2024, NIST Atomic Spectra Database (ver. 5.12), [Online]. Available: `https://physics.nist.gov/asd` [2025, September 2]. National Institute of Standards and Technology, Gaithersburg, MD.

Labbé, I., Oesch, P. A., Bouwens, R. J., et al. 2013, ApJL, 777, L19, doi: 10.1088/2041-8205/777/2/L19

Labbé, I., van Dokkum, P., Nelson, E., et al. 2023a, Nature, 616, 266, doi: 10.1038/s41586-023-05786-2

Labbé, I., Greene, J. E., Bezanson, R., et al. 2023b, arXiv e-prints, arXiv:2306.07320, doi: 10.48550/arXiv.2306.07320

Labbe, I., Greene, J. E., Matthee, J., et al. 2024, arXiv e-prints, arXiv:2412.04557, doi: 10.48550/arXiv.2412.04557

Lambrides, E., Garofali, K., Larson, R., et al. 2024, arXiv e-prints, arXiv:2409.13047, doi: 10.48550/arXiv.2409.13047

Lambrides, E., Larson, R., Hutchison, T., et al. 2025, arXiv e-prints, arXiv:2509.09607, doi: 10.48550/arXiv.2509.09607

Leung, G. C. K., Finkelstein, S. L., Pérez-González, P. G., et al. 2024, arXiv e-prints, arXiv:2411.12005, doi: 10.48550/arXiv.2411.12005

Lin, X., Wang, F., Fan, X., et al. 2024, ApJ, 974, 147, doi: 10.3847/1538-4357/ad6565

Lin, X., Fan, X., Cai, Z., et al. 2025a, arXiv e-prints, arXiv:2507.10659, doi: 10.48550/arXiv.2507.10659

—. 2025b, arXiv e-prints, arXiv:2507.10659, doi: 10.48550/arXiv.2507.10659

Lotz, J. M., Koekemoer, A., Coe, D., et al. 2017, ApJ, 837, 97, doi: 10.3847/1538-4357/837/1/97

Ma, Y., Greene, J. E., Setton, D. J., et al. 2025, ApJ, 981, 191, doi: 10.3847/1538-4357/ada613

Maiolino, R., Scholtz, J., Curtis-Lake, E., et al. 2023, arXiv e-prints, arXiv:2308.01230, doi: 10.48550/arXiv.2308.01230

Marinello, A. O. M., Rodriguez-Ardila, A., Garcia-Rissmann, A., Sigut, T. A. A., & Pradhan, A. K. 2016, arXiv e-prints, arXiv:1602.05159, doi: 10.48550/arXiv.1602.05159

Matthee, J., Naidu, R. P., Brammer, G., et al. 2023, arXiv e-prints, arXiv:2306.05448, doi: 10.48550/arXiv.2306.05448

Naidu, R. P., Matthee, J., Kramarenko, I., et al. 2024, arXiv e-prints, arXiv:2410.01874, doi: 10.48550/arXiv.2410.01874

Naidu, R. P., Matthee, J., Katz, H., et al. 2025, arXiv e-prints, arXiv:2503.16596, doi: 10.48550/arXiv.2503.16596

Oke, J. B. 1974, ApJS, 27, 21, doi: 10.1086/190287

Osterbrock, D. E. 1989, Astrophysics of gaseous nebulae and active galactic nuclei

Osterbrock, D. E., & Ferland, G. J. 2006, Astrophysics of gaseous nebulae and active galactic nuclei

Pasha, I., & Miller, T. B. 2023, The Journal of Open Source Software, 8, 5703, doi: 10.21105/joss.05703

Reddy, N. A., Kriek, M., Shapley, A. E., et al. 2015, ApJ, 806, 259, doi: 10.1088/0004-637X/806/2/259

Reddy, N. A., Oesch, P. A., Bouwens, R. J., et al. 2018, ApJ, 853, 56, doi: 10.3847/1538-4357/aaa3e7

Richards, G. T., Strauss, M. A., Fan, X., et al. 2006, AJ, 131, 2766, doi: 10.1086/503559

Rigby, J., Perrin, M., McElwain, M., et al. 2023, PASP, 135, 048001, doi: 10.1088/1538-3873/acb293

Rinaldi, P., Bonaventura, N., Rieke, G. H., et al. 2025a, ApJ, 992, 71, doi: 10.3847/1538-4357/adfa10

Rinaldi, P., Rieke, G. H., Wu, Z., et al. 2025b, arXiv e-prints, arXiv:2507.17738, doi: 10.48550/arXiv.2507.17738

Rudy, R. J., Mazuk, S., Puetter, R. C., & Hamann, F. 2000, ApJ, 539, 166, doi: 10.1086/309222

Rusakov, V., Watson, D., Nikopoulos, G. P., et al. 2025, arXiv e-prints, arXiv:2503.16595, doi: 10.48550/arXiv.2503.16595

Sabti, N., Muñoz, J. B., & Kamionkowski, M. 2024, PhRvL, 132, 061002, doi: 10.1103/PhysRevLett.132.061002

Saldana-Lopez, A., Chisholm, J., Gazagnes, S., et al. 2025, MNRAS, doi: 10.1093/mnras/staf1680

Setton, D. J., Greene, J. E., de Graaff, A., et al. 2024, arXiv e-prints, arXiv:2411.03424, doi: 10.48550/arXiv.2411.03424

Sigut, T. A. A., & Pradhan, A. K. 1998, ApJL, 499, L139, doi: 10.1086/311369

—. 2003, ApJS, 145, 15, doi: 10.1086/345498

Stark, D. P., Ellis, R. S., Bunker, A., et al. 2009, ApJ, 697, 1493, doi: 10.1088/0004-637X/697/2/1493

Steinhardt, C. L., Jauzac, M., Acebron, A., et al. 2020, ApJS, 247, 64, doi: 10.3847/1538-4365/ab75ed

Tang, M., Stark, D. P., Plat, A., et al. 2025, arXiv e-prints, arXiv:2505.06359, doi: 10.48550/arXiv.2505.06359

Taylor, A. J., Kokorev, V., Kocevski, D. D., et al. 2025, arXiv e-prints, arXiv:2505.04609, doi: 10.48550/arXiv.2505.04609

Torralba, A., Matthee, J., Pezzulli, G., et al. 2025, arXiv e-prints, arXiv:2510.00103, doi: 10.48550/arXiv.2510.00103

Tripodi, R., Bradač, M., D'Eugenio, F., et al. 2025, arXiv e-prints, arXiv:2507.20684, doi: 10.48550/arXiv.2507.20684

Valentino, F., Brammer, G., Gould, K. M. L., et al. 2023, arXiv e-prints, arXiv:2302.10936, doi: 10.48550/arXiv.2302.10936

Volonteri, M., Trebitsch, M., Greene, J. E., et al. 2025, A&A, 695, A33, doi: 10.1051/0004-6361/202451963

Wang, B., Fujimoto, S., Labbe, I., et al. 2023, arXiv e-prints, arXiv:2308.03745, doi: 10.48550/arXiv.2308.03745

Wang, B., Leja, J., de Graaff, A., et al. 2024, arXiv e-prints, arXiv:2405.01473, doi: 10.48550/arXiv.2405.01473

Wang, B., de Graaff, A., Davies, R. L., et al. 2025, ApJ, 984, 121, doi: 10.3847/1538-4357/adc1ca

Whalen, K. E., Weaver, K. A., Hickox, R. C., & Lambrides, E. 2025, arXiv e-prints, arXiv:2509.21236, doi: 10.48550/arXiv.2509.21236

Yue, M., Eilers, A.-C., Ananna, T. T., et al. 2024, ApJL, 974, L26, doi: 10.3847/2041-8213/ad7eba

Zitrin, A., Fabris, A., Merten, J., et al. 2015, ApJ, 801, 44, doi: 10.1088/0004-637X/801/1/44